UNIVERSITÀ DEGLI STUDI DI CATANIA
DOTTORATO DI RICERCA IN INGEGNERIA FISICA

Vincenzo Costa

Study of protoplanet migration processes in sub-Keplerian conditions through SPH hydrodynamic simulations

Il Tutor
prof. V. Pirronello

Il Coordinatore
prof. G. Giaquinta

TESI PER IL COSEGUIMENTO DEL TITOLO

XXIII Ciclo 2007-2010

Introduction

The interest on the formation processes of planetary systems has been growing for the last years, due to the improvements on the observational techniques used to detect extra-solar planets. According to current theories, protoplanets-disc interaction plays a major role in determining the final masses and orbits of the newly born planets. This interaction is considered responsible for the migration of protoplanets towards the central star. The formation of giant planets (Jupiter like) in particular should be contextual to their quick migration on a time-scale in the order of 10^5 years. Such a time-scale should be smaller by an order of magnitude than that of gas accretion onto the protoplanet during the hierarchical growing-up of protoplanets by collisions with other minor objects. These arguments have been analysed recently using N-body and/or fluid-dynamics simulations or a mixing of them. In this work, inviscid 2D simulations are performed, using the SPH method, to study the migration of one or two protoplanets, to evaluate the effectiveness of the accretion disc in the protoplanet dragging towards the central star, as a function of the mass of the planet(s) and of the disc tangential kinematics (angular momentum). To this purpose, the SPH scheme is considered suitable to study the roles of turbulence, kinematic and boundary conditions, due to its intrinsic advective turbulence, especially in 2D and in 3D codes. Concerning the kinematic conditions of the protoplanetary accretion disc, a Keplerian distribution of the gas particles velocities is a common assumption. But consistent deviations from a perfect Keplerian kinematics, with up to $30-40\%$ lower than Keplerian values for angular momentum, are often currently observed in collisional flows where an accretion protoplanetary disc surrounds the central protostar. From a theoretical point of view, both pressure forces and dissipative effects due to shock occurrence in accretion processes, produce a general sub-Keplerian kinematics, even in non viscous fluid dynamics.

Simulations are performed here both in disc sub-Keplerian and in Keplerian kinematic conditions. The aim is to develop a parameter study of protoplanetary migration if moderate and consistent deviations from Keplerian Kinematics occur.

In the case of a single planet, the results of this work show migration times of a few orbital periods for Earth-like planets in sub-Keplerian conditions, while for Jupiter-like planets estimates suggest that about 10^4 orbital periods occur until the orbital size (semi-major axis) is reduced to about a half of its initial value. Time-scales of planet migration are strongly dependent on the relative position of the planet with respect to the shock region near the centrifugal barrier of the disc flow.

In the case of two-planets systems, the dynamical evolution of the two protoplanets embedded in a 2D non viscous sub-Keplerian accretion disc is here investigated, according to several initial conditions, to pay attention to the radial transport of a system of two mutually interacting solid bodies. Results show a quite general radial migration of the two protoplanets towards the inner radial zones of the disc. In sub-Keplerian disc kinematics the time-scale of the whole radial transport is mainly ruled by planet-disc interaction, despite the possible presence of a Jovian mass planet. Gravitational radial oscillations (GRO) of each component of the two-planets system are observed as expected, especially in systems with two Jovian planets. These oscillations are functions of planet masses, mutual separation and radial distance to the central star. Moreover, each protoplanet is secularly affected by the disc drag with a consequent migration towards the central star. Details of each case are described further in the next chapters.

Chapter 5 in particular is focused on the dissipative effect of the artificial viscosity present in numerical model used for this work. Even if not directly connected to the main topic of this thesis, the study gives an important contribution in understanding one of the main physical and numerical features of the used hydrodynamic code.

Chapter 1

Protoplanet migration in accretion discs

1.1 Main features of planetary migration

Currently, nearly 300 extra-solar planets (http://www.exoplanets.eu/) have been detected, and most of them are massive, Jupiter-like, planets with small (less than one Astronomical Unit) semi-major axes (see Perryman, 2000; Udry and Santos, 2007, for a review on detection methods and on the main properties of exo-planets). According to current theories, planets are formed through a hierarchical growing up via capture of gas, dust and greater bodies. This requires the presence of enough matter at the protoplanet location (orbit). There is common agreement on the fact that, at distances below 1 AU, there would not be enough material to form a giant planet. Therefore, protoplanets are likely formed at greater distances from the central star, and then the interaction of each protoplanet with the protoplanetary accretion disc is responsible for changes in the orbital parameters, particularly the orbital size (planet migration).

If the semi-major axis of a protoplanet has to decrease (inward migration), a transfer of angular momentum, from the protoplanet to the accretion disc material, has to occur.

Theoretical models for the formation of planetary systems are mostly based on the crucial role of an accretion disc around a forming young star, where the disc provides both the material for the forming planets and the interactions responsible for the migration of the protoplanets towards the central star. Therefore the detailed understanding of migration mechanisms appears mandatory in order to build self-consistent models for planetary systems formation.

One possible way of transferring angular momentum between a protoplanet and the accretion disc is through gravitational interaction. Central forces cannot change the angular momentum of an orbiting body, but if the structure of the accretion disc is not axially symmetric, the combined gravitational action of all gas and dust particles forming the disc can produce a net torque on the protoplanet. This hypothesis has been analytically investigated by Goldreich and Tremaine (1979, 1980); Papaloizou and Lin (1984); Lin and Papaloizou (1986a,b); Ward (1997). They suggest that gravitational torques due to resonant non-axisymmetric structures could act to transfer angular momentum between the protoplanets and the disc. The gravitational disturbance exerted by a protoplanet on the disc produces spiral density waves which break the axial symmetry of the disc structure. Perturbation theory allows an estimate of the net torque that this perturbed disc exerts back onto the planet at "Lindblad resonance sites" (Goldreich and Tremaine, 1980; Ward, 1997). This disc-planet interaction induces also a repulsion of material on either side of the protoplanet's orbit, with a possible formation of a lower density region along the orbit with respect to the surrounding disc structure (*density gap*), depending on the interaction strength.

Two main migration types are then distinguished:

- *type I* (Tanaka et al., 2002), when an Earth-like planet, not capable of

opening a density gap in the disc is embedded in the disc structure. In this case the migration rate is proportional to the protoplanet mass;
- *type II*, when a massive protoplanet, capable of opening and maintaining a density gap, remains trapped in this gap. In this case migration is due to the viscosity dominated evolution of the disc. In both cases it is possible that the lifetime of migration is shorter than the lifetimes of planet formation or disc dissolution, causing the collapse of the planet toward the star.
More recently (Papaloizou et al., 2007) a *type III* migration mechanism has been suggested. In this case the main migration "engine" is provided by material flowing through the co-orbital region of the protoplanet. This material would change orbit (and angular momentum) while passing trough the co-orbital region, exerting a torque on the protoplanet. This torque can be evaluated trough momentum conservation.

It is clear that analytical predictions for the behaviour of a system consisting of gas, dust and forming planets, need accurate numerical simulations to be confirmed and/or improved (Papaloizou et al., 2007). Several papers devoted to this theme, according to various fluid-dynamics schemes, showed that type I and type II mechanisms can be very effective, according to planet mass, for the protoplanet dragging toward the central protostar. Characteristic time-scales are in the order of 10^5 years (Artymowicz, 2004; D'Angelo et al., 2002, 2003, 2006; Kley, 2000; Papaloizou et al., 2007; Schäfer et al., 2004).

The classification of protoplanets migration mechanisms described above, is based on some typical assumptions on the structure of protoplanetary discs. The most important is the *Keplerian hypothesis*, according to which the velocities of the gas particles in the disc, are distributed in a Keplerian way, as if each particle were orbiting under the action of a central gravitational force alone, according to its distance to the central star.
When building a numerical model for a protoplanetary accretion disc, it is

difficult to select proper initial conditions, and a the Keplerian condition is usually considered a simple and acceptable choice (Cresswell and Nelson, 2006; de Val-Borro et al., 2006; Kley, 2000; Schäfer et al., 2004; Terquem et al., 2000). Nevertheless, there are reasons to believe that a Keplerian distribution of velocities cannot survive under the action of pressure forces (which are often neglected), dissipative effects and the presence of one or more protoplanets. This will be better discussed further in the next chapters. Moreover, most of the published articles discard the inelastic accretion of gas onto the planets. However, from the theoretical point of view, both pressure forces and dissipative processes are able to produce a deviation from a pure Keplerian configuration.

The main aim of this work is to study the role of initial and boundary conditions on planetary migration as a consequence of planet-disc dynamic interaction during the initial formation phases of stellar systems. Other authors have already started exploring the effects of sub-Keplerian flows for a wider context (like formation and evolution of Active Galactic Nuclei) during the accretion disc formation phase (Sollins and Ho, 2005; Ulrich, 1976) or for small sub-Keplerian corrections due to the contribution of pressure gradients (Paardekooper and Mellema, 2004). It is then useful to study here the role of sub-Keplerian flows as an open possibility for stars pre-main sequence accretion processes, as well as their role in the radial transport of solid bodies forming and orbiting inside the protostar's accretion disc. In section 2.2 a detailed explanation of the parameters involved in this study is given.

Non viscous Cartesian 2D SPH sub-Keplerian disc models are described in the following chapters, and resulting planetary migration times both for Jovian and for Terrestrial planets are then reported. Models with Jovian or Terrestrial protoplanets, interacting with an initial Keplerian accretion disc, are also produced for comparison.

1.1.1 Protoplanet survival

The migration mechanisms leading the protoplanets towards the central star could, in principle, drag the planets towards a final fall and capture by the star. There must be some way to stop the dragging at the distances where planets are actually observed in real planetary systems.

The presence of sub-Keplerian flows inside an accretion disc may lead to the formation of shock fronts. The formation of steady or progressive shock fronts and complex turbulent structures in sub-Keplerian accretion flows in AGN, was described in Chakrabarti and Molteni (1993); Molteni et al. (1994); Lanzafame et al. (1998). These can produce pulsed or periodic outflows, as described by Lanzafame et al. (2008) as a consequence of collisional interactions in the disc surrounding the central accreting object. In such environments (AGN or equivalently protostellar systems), the potential importance of the centrifugal barrier in developing outflow structures in turbulent collisional fluid-dynamics, was successfully described in those papers. This implies that the possibility of a slowing of the protoplanets drag toward the central star cannot be excluded in principle. This effect, if present in protoplanetary systems, might play an important role in the survival of the forming planets, because it could contribute to the "braking" of planet migration. Therefore, as a secondary aim, the purpose of this work is the methodical search for those initial and boundary conditions determining results showing how Jovian and Terrestrial protoplanets could stay in orbits surrounding the central stars at distances of the order of that of Venus or Mercury, as observed in many of the detected exo-planetary systems.

1.2 Two-planets systems

The main part of this study is focused on the migration processes affecting one single protoplanet embedded inside an accretion disc, for the examination of sub-Keplerian kinematic conditions on protoplanetary systems and their effect on planetary migration. As a second a part of this study, systems with more than one protoplanet are taken into account.

The investigation of the kinematic evolution of two (or more) protoplanets embedded in a protostellar disc has also been reported in Cresswell and Nelson (2008); Crida et al. (2007, 2008); Jiang and Yeh (2007); Kley et al. (2004, 2005); Kominami et al. (2005); Lecoanet et al. (2009); Nelson and Papaloizou (2002); Papaloizou (2003); Pierens and Nelson (2008), whose aim is the discovery of correlations and/or constraints relative to planetary *mean motion resonances*[1], together with the damping of orbital parameters during the migration processes within a Keplerian gaseous environment. Since the formation of resonant two-planets systems is considered possible as the result of joint orbital evolution of the two protoplanets within the accretion disc, it is worth studying two-protoplanets systems here. The aim is to broaden the analysis of the effect of sub-Keplerian kinematic conditions of the accretion disc on a system of two bodies in the central star gravitational field, where the mutual interaction between the two protoplanets is both direct (gravitational) and indirect, through the effect on one planet of the dynamical changes in the disc structure produced by the other planet, like possible shock waves.

Thus, several 2D SPH models of two accreting protoplanets within sub-Keplerian flows were developed. They are analysed here to study how dou-

[1] A *resonance* in a planetary system is a combination of orbits whose orbital periods are in a ratio expressed with small integer numbers, like 2 : 1 or 3 : 1. Such resonances were observed (Crida et al., 2008) in many detected exo-planetary systems, and some simulations were made to explain their formation and evolution (Kley et al., 2005; Lecoanet et al., 2009).

ble planetary migration evolves according to initial and boundary conditions of the accretion disc, and according to the protoplanet masses. In this approach, particularly interesting is the model where an external Terrestrial and internal Jovian protoplanets characterise the initial choice, since, as it will be shown in the next chapters, Terrestrial planets migrate much faster. Then, an initially external Terrestrial protoplanet would migrate to an orbit close to the companion Jovian planet's orbit, with the risk of a capture or a "slingshot effect", or an abrupt deviation towards eccentric orbits of the lighter protoplanet. Since two-planets models are still under analysis and development, only the main features will be briefly discussed, concerning specifically the differences in the orbital evolution of the two protoplanets when different combination of masses and disc gas sub-Keplerian angular momentum are used as initial conditions. Discussions and deeper studies concerning resonances will be left for a future work.

Chapter 2

Models features and boundary conditions

2.1 Models

2.1.1 The SPH method

The simulations presented in this work are based on a two-dimensional model which makes use of the Smoothed Particle Hydrodynamics (SPH) numerical method (Monaghan, 1992).

The SPH is an interpolation method that evaluates a physical quantity A at a point in space, by interpolating its values at other positions around the given point:

$$A(\mathbf{r}) = \int A(\underline{\mathbf{r}})W(\mathbf{r} - \underline{\mathbf{r}}, h)d\underline{\mathbf{r}} \tag{2.1}$$

where W is the *interpolation kernel*, h is the *smoothing length* and the integration is taken over the entire "space" (computational domain). The interpolation kernel is a function of position, whose integral over the entire space is normalised to 1, and its profile is usually "peaked" around the origin and it goes to zero at infinity. It satisfies the condition:

$$lim_{h\to 0}W(\mathbf{r} - \underline{\mathbf{r}}, h) = \delta(\mathbf{r} - \underline{\mathbf{r}}) \tag{2.2}$$

The width of the peak is of the order of the smoothing length h, and it defines the spatial resolution of the numerical method.

In a real numerical application the integration must be discretised, each quantity is then calculated at a finite number of positions, corresponding to Lagrangian "particles". The following expression is used for relation 2.1:

$$A(\mathbf{r}) = \sum_j m_j \frac{A_j}{\rho_j} W(\mathbf{r} - \mathbf{r_j}, h) \tag{2.3}$$

where each j denotes a particle index and the summation should be taken over all particles. Actually, given the peaked profile of the interpolation kernel, in numerical codes the summation is done on a limited group of particles located around the position $\mathbf{r}$. In the models used in this work the kernel is a 3rd order polynomial.

One of the main advantages of this numerical method with respect to other finite difference methods, is the easy way of evaluating derivatives. Since the kernel function is usually analytically differentiable, each derivative of a given physical quantity is evaluated through the derivative of the kernel. For example:

$$\nabla_r A(\mathbf{r}) = \sum_j m_j \frac{A_j}{\rho_j} \nabla_r W(\mathbf{r} - \mathbf{r_j}, h) \tag{2.4}$$

The SPH expressions for the hydrodynamics equations, used to evaluate the physical quantities at the position corresponding to the ith SPH particle, are:

$$\rho_i = \sum_j m_j W_{ij} \tag{2.5}$$

$$\frac{d\mathbf{v}_i}{dt} = -\sum_j m_j \left(\frac{p_j}{\rho_j^2} + \frac{p_i}{\rho_i^2} + \Pi_{ij} \right) \nabla_i W_{ij} \tag{2.6}$$

$$\frac{du_i}{dt} = \frac{1}{2} \sum_j m_j \left(\frac{p_j}{\rho_j^2} + \frac{p_i}{\rho_i^2} \right) \mathbf{v}_{ij} \cdot \nabla_i W_{ij} \tag{2.7}$$

where the term W_{ij} is a compact expression for $W(\mathbf{r_i} - \mathbf{r_j}, h)$ and $\mathbf{v}_{ij} = \mathbf{v}_i - \mathbf{v}_j$. Mass conservation is expressed by eq. (2.5) (continuity equation);

momentum conservation by eq. (2.6); energy conservation by eq. (2.7), where u_i is the *thermal energy per unit mass*.

When actually evaluating the above summations, the effective addends are those concerning “neighbour” particles, due to the peculiar shape of the interpolating kernel, as explained above. These neighbours are located within a given distance (usually in the order of $2h$) from particle i. In eq. (2.6) the term Π_{ij} is a pressure contribution due to *artificial viscosity*. This component is necessary, even if the original physical equations are inviscid (Euler equations), in order to be able to correctly resolve gas shocks numerically, to avoid spurious heating and to handle fluid discontinuities:

$$\Pi_{ij} = \begin{cases} \frac{-\alpha \bar{c}_{ij} \mu_{ij} + \beta \mu_{ij}^2}{\bar{\rho}_{ij}} & \mathbf{v}_{ij} \cdot \mathbf{r}_{ij} < 0 \\ 0 & \mathbf{v}_{ij} \cdot \mathbf{r}_{ij} > 0 \end{cases} \tag{2.8}$$

where

$$\mu_{ij} = \frac{h \mathbf{v}_{ij} \cdot \mathbf{r}_{ij}}{\mathbf{r}_{ij}^2 + \eta^2} \tag{2.9}$$

The linear α and quadratic β artificial viscosity terms are usually set to 1 when handling accretion discs, and this choice is confirmed here. The parameter η is used to avoid problems with smoothing in high density region, and it is set to $0.1h$. As it appears from eq. (2.8), the artificial viscosity gives a contribution during compression ($\mathbf{v}_{ij} \cdot \mathbf{r}_{ij} < 0$), and it is zero otherwise.

The choice of using the SPH method is funded on the grounds of its Lagrangian nature and its ability to easily tackle hydrodynamic problems with free surfaces. Moreover, when describing planet-gas interactions, the use of SPH has a comparable performance respect to other grid-based and particle methods, as explained by de Val-Borro et al. (2006). Given the lack of a wide range of case studies on the matter in SPH, especially concerning the analysis of sub-Keplerian flows, this work gives an interesting contribution to improve the basic knowledge on disc-protoplanet interaction.

2.1.2 Interactions and physical units

The choice of referring to the Euler hydrodynamic equations is due to the aim of this work to study the effect of sub-Keplerian initial conditions on the accretion disc evolution. The inviscid nature of the gas simplify the analysis of the various kinematic conditions. The eventual presence of physical viscosity would make the outcoming results more difficult to read, and the development of viscous models will be left for a future work.
The hydrodynamic equations are coupled to an equation of state of the gas. The equation of state used here is:

$$P = (\gamma - 1)\rho u \tag{2.10}$$

where u is the thermal energy per unit mass, γ is the polytropic index, which is set to 5/3 (ideal gas equation) for the present work. If radiation, partial molecular dissociation or partial ionisation effects have to be simulated, the parameter γ can be adjusted to values lower than 5/3, giving the overall effect of a higher compressibility to the gas. A detailed radiation treatment is not yet included in the code.
The model is built in Cartesian coordinates and dimensionless quantities are used, in order to give a more general applicability to the results, and to make the numerical treatment of the model easier. The reference physical units are:

- the initial stellar mass M_0;
- the stellar radius R_0;
- the Keplerian period of an orbit of radius R_0 around a star of mass M_0:
  $T_0 = \frac{2\pi}{\sqrt{GM_0}} R_0^{3/2}$

All other physical quantities are referred to the above specified units. Here are other main conversion units that can be used to convert the dimensionless results:

- velocity: $v_0 = \frac{1}{2\pi}\sqrt{\frac{GM_0}{R_0}}$
- specific angular momentum: $j_0 = \frac{1}{2\pi}\sqrt{GM_0 R_0}$
- energy per unit mass: $u_0 = \frac{1}{4\pi^2}\frac{GM_0}{R_0}$
- surface density: $\Sigma_0 = \frac{M_0}{R_0^2}$

The initial conditions used to build the accretion disc are axially symmetric, but the same symmetry is not assumed in the subsequent dynamical evolution, and the disc is free to evolve in a 2D environment according to the hydrodynamic equations.

In order to build the accretion disc, the simulation is started with no particles, then SPH particles are created at fixed positions in space. These positions are conventionally referred to as *injectors*. They are located along a circle concentric with the central star, with a radius nearly equal to the maximum extension of the computational domain (see section 2.2 for details), and the distance between the injectors is set to $4h$.

At every time step, a new particle is generated at the position of each injector, but only if there are no particles inside a circle centred in the injector an with a radius equal to $2h$. The generated particles have initial tangential velocities set by choosing a value for the angular momentum per unit mass j, which is one of the free parameters. The above explained particle generation method, and the choice of sub-Keplerian values for j produces a stable flux of particles whose inflow progressively fill the space around the central star, thus forming and populating the accretion disc.

At some point, the accretion disc reaches a “nearly” steady state population of particles (time averaged since some variation of the number of particles and of the density distributions are actually observed during the simulations, due to the highly turbulent nature of the calculated flows) with $3 \times 10^5 - 5 \times 10^5$ particles, depending on the model. This result is obtained using a smoothing length $h = 0.3$. At this stage, the planet is inserted and the model is evolved further. The following interactions are included:

1. gravitational interaction between gas particles and central star;
2. gravitational interaction between planet(s) and star;
3. gravitational interaction between particles and planet(s);
4. gravitational interaction between planet and planet (for two-planets models only);
5. gas pressure between neighbouring gas particles;
6. artificial viscosity (pressure contribution) between gas particles;
7. gas particle capture by the planet (conservation of momentum is used to correct the planet speed before removing the particle) when gas particles approach the planet area (planet-particle distance less than $2h$).

2.1.3 Pseudo-atmosphere

The above listed interactions do not include the eventual contribution due to the pressure exerted between the gas and the protoplanet surface. The chosen numerical approach and resolution ($h = 0.3$) do not allow a detailed treatment of this type of interaction, since the protoplanet is nearly point-like in this context. Nevertheless, a simplified approach to include an estimate of this pressure contribution is used here. An "ad hoc" SPH gas particle at the protoplanet position is added, giving to it the planet's velocity and the mass of the other surrounding gas particles. Densities and pressures of all gas particles are then calculated, including the special particle representing the planet, according to the SPH method, as if this special particle were a part of the disc gas. The pressure of planet particle is then taken as an approximate estimate of the pressure acting on the planet. Though this approach, which is hereafter indicated as adding a "pseudo-atmosphere" to the protoplanet, may appear simplistic, it allows the introduction of the, otherwise totally missing, pressure interaction acting on the planet. This approach is not applied to all models. Some models include it and some do not, allowing an evaluation of the importance of this effect on the evolution of the protoplanet orbit.

2.1.4 Mass of the disc and self-gravity

The mass given to each SPH particle is 10^{-11} (dimensionless units), a value that, with a total number of particles in the order of $\sim 10^5$ gives a total mass of the disc of $\sim 10^{-6}$. Since this mass is referred to the stellar mass M_0, the dominating gravitational force in such a system is still due to the central star, and in second order, to the still fundamental gravitational force due to the protoplanet (or the protoplanets). Therefore, it is safe to discard the self-gravity of the disc, at least for the purposes of the present work.

The specified choice for the disc mass can be considered realistic. Reported values for disc masses are in fact in the range $10^{-3} - 10^{-1}\ M_\odot$ on the grounds of observational constraints from T-Tauri stars (Hartmann, 2000; Terquem et al., 2000), but this value is usually distributed over a disc with a radius of $100 - 1000\ AU$. In order to compare this to the structure of the simulated discs, given the dimensionless nature of the simulation, some physical reference units must be chosen. If 1 $M_\odot$ and 2-3 $R_\odot$ are taken for a typical T-Tauri star (Bertout, 1989), the disc has a dimension of about ~ 2 AU. Therefore, the simulations presented here cover only the central part of a typical T-Tauri accretion disc, and the mass included in the simulation is in agreement with observational constraints.

2.1.5 The inviscid choice

Most accretion disc models in literature include viscosity, according to the disc model of Shakura and Sunyaev (1973). Nevertheless, even today it is hard to find a self-consistent way to give a correct value for the viscosity parameter (indicated with α_{SS} in Shakura and Sunyaev (1973) model). Here, the effect of physical viscosity is not the primary concern, since the analysis of this work is focused on protoplanet migration mechanisms based on gravitational and pressure forces and momentum transfer through gas particle captures. Thus, the models developed here are inviscid. The absence of physical viscosity enhances the turbulent nature of the simulations, allowing a correct description of some effects due to turbulence, like the development of non-axisymmetric structures in the disc (induced also by the presence of the protoplanet). Turbulence can also produce stronger shock fronts when infalling gas particles hit the centrifugal barrier.

Another consequence of the absence of physical viscosity is the fact that the protoplanet migration occurring in current simulations cannot be explained in terms of pure type II migration described in the introduction, since this mechanism is specifically "viscosity driver". Comparison of the results obtained here with the typical effects of type II migration is interesting anyway, as better explained in chapter 4.

A deeper analysis on some peculiar features of the artificial viscosity which is used in this work, is carried out in chapter 5, where a study on the dissipative effects on artificial viscosity is carried out and discussed.

2.2 Initial conditions

One of the free parameters of the model is the angular momentum per unit mass j given to the injected particles. The injectors are located at a distance of 130 from the central star, and three choices are made here for j:

18, 36, 54.

All the three choices give a sub-Keplerian kinematics to the velocity distribution of the accretion disc (particles injected at a radial distance of 130 would have Keplerian velocity with $j \sim 70$), therefore the injected particles start decreasing their distance to the centre, until they "hit" the centrifugal barrier. These choices allow a parametric study ranging from "extreme" ($j = 18$) to "weak" ($j = 54$) sub-Keplerian initial conditions.

Two different masses are chosen for the planets: 10^{-7}, representing Earth-like planets, and 10^{-3} for Jupiter-like planets. The computational domain is circular, extended in the xy plane with a radius of 150, with the star located in the "origin". For the single planet models, the initial position of the planet is at $X_p = 100$ and $Y_p = 0$, while for the models including two protoplanets, the two initial positions are: $X_1 = 70$ (internal protoplanet) and $X_2 = 100$ (external protoplanet), with $Y = 0$ for both of them. In all cases the initial eccentricity is set to zero, thus building initial circular orbits.

2.2.1 Initial density profile and accretion rate

The azimuthally averaged density profiles of the sub-Keplerian accretion discs, just before planet insertion, are plotted in fig. 2.1 for the three cases ($j = 18, 36, 54$). A density peak is present near the centrifugal barrier in each case. For $j = 18$ the peak is close to the star, while for higher j values the density close to the star has values similar to those found at the disc outer edge. Density in SPH is computed according to local particle mass distribution. At the disc outer edge, particles are produced and injected in the stellar gravitational potential well. Instead particles are in a free fall very close to the central star, where gravitational potential rules the whole gas dynamics, and they are "removed" from the simulation (the mass of the particle is added to the star mass) when they reach a radial position equal

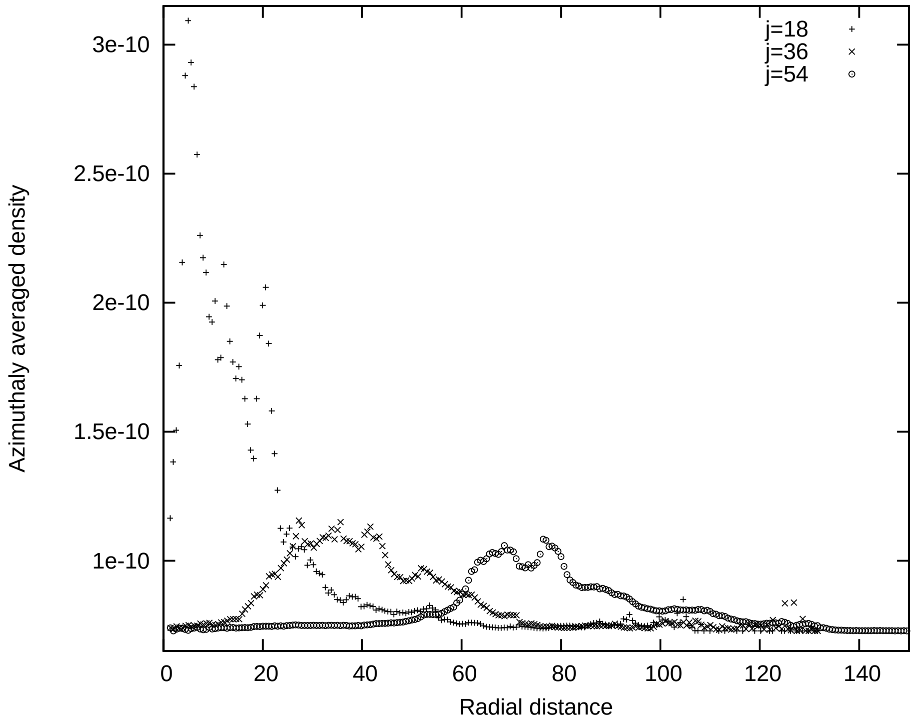

Figure 2.1: Azimuthally averaged density profiles of the sub-Keplerian accretion discs, just before planet insertion, for $j = 18, 36, 54$.

to the star radius.

As far as the disc material accretion rate onto the central star, if 1 $M_\odot$ and 2-3 $R_\odot$ are taken for a typical T-Tauri star (Bertout, 1989), we obtain for the three cases values of $2 \times 10^{-6},\ 6 \times 10^{-7},\ 3 \times 10^{-7}\ M_\odot y^{-1}$ with oscillations of about $30\%, 80\%, 100\%$ respectively. These values are in agreement with estimated accretion rates for T-Tauri stars (Gullbring et al., 1998; Hartigan et al., 1995).

The above specified oscillations in the accretion rate are directly linked to the turbulent nature of the disc models, as it is evidenced by the high value of the Reynolds number, evaluated by using the artificial viscosity coefficient $\nu_{num} = c_s h$ (Molteni et al., 1991), especially at the disc outer edge. We have values of the Reynolds number of about 1200, 2400, 3600 for $j = 18, 36, 54$ respectively. Instead, in the innermost regions, where the disc gas temperature is higher, Re values of about $300 \div 1000$ are still evaluated.

In order to compare some of the results with more traditional models, some computations (two with an Earth-like planet and two with a Jupiter-like planet) are built using an initial exactly Keplerian distribution of gas particle velocities, with an initial uniform density over the entire disc area. For simplicity, these models are referred to as "Keplerian", even if the velocity distribution of the gas particles cannot remain exactly Keplerian during the simulation, due to the pressure forces within the gas and to the interaction between the planet and the accretion disc. These models will be used to test the eventual formation of a density gap near the protoplanet location, and to compare some classical views on the subject (Ward, 1997) with the results obtained here using an inviscid model.
A summary of the distinguishing features of the models is given in tables 2.1 and 2.2 together with identifying labels.

In the tables, the specific initial angular momentum j of the injected particles is reported in the second column. For the models with one protoplanet (table 2.1) the single protoplanet mass is specified in the third column, units of central star mass, and the eventual presence of the "pseudo-atmosphere" (section 2.1.3) is also indicated (fourth column). For two-protoplanets systems (table 2.2), the masses of the two protoplanets are reported in the third (internal planet) and fourth (external planet) columns respectively. The grid of two-planets models is not as complete as the one for single planet systems. Models with two protoplanets including the pseudo-atmosphere are not present, and the extreme sub-Keplerian case with $j = 18$ is not included either.

Label	j	M_p	pseudo-atmosphere
18a	18.0	10^{-3}	no
18b	18.0	10^{-3}	yes
18c	18.0	10^{-7}	no
18d	18.0	10^{-7}	yes
36a	36.0	10^{-3}	no
36b	36.0	10^{-3}	yes
36c	36.0	10^{-7}	no
36d	36.0	10^{-7}	yes
54a	54.0	10^{-3}	no
54b	54.0	10^{-3}	yes
54c	54.0	10^{-7}	no
54d	54.0	10^{-7}	yes
kepl_a	71.6	10^{-3}	no
kepl_b	71.6	10^{-3}	yes
kepl_c	71.6	10^{-7}	no
kepl_d	71.6	10^{-7}	yes

Table 2.1: List of computed models with one single protoplanet, with their identifying labels (first column); the second column gives the specific angular momentum $j$of injected gas particles; the third column gives the initial mass of the protoplanet; the fourth column indicates the eventual presence of the pseudo-atmosphere on the protoplanet.

Label	j	M_1	M_2
2_36a	36.0	10^{-3}	10^{-3}
2_36b	36.0	10^{-7}	10^{-3}
2_36c	36.0	10^{-3}	10^{-7}
2_36d	36.0	10^{-7}	10^{-7}
2_54a	54.0	10^{-3}	10^{-3}
2_54b	54.0	10^{-7}	10^{-3}
2_54c	54.0	10^{-3}	10^{-7}
2_54d	54.0	10^{-7}	10^{-7}
2_kepl_a	71.6	10^{-3}	10^{-3}
2_kepl_b	71.6	10^{-7}	10^{-3}
2_kepl_c	71.6	10^{-3}	10^{-7}
2_kepl_d	71.6	10^{-7}	10^{-7}

Table 2.2: List of computed models with two protoplanets, with their identifying labels (first column); the second column gives the specific angular momentum j of injected gas particles; the third column gives the initial mass of the internal (initial distance equal to 70) protoplanet; the fourth column gives the initial mass of the external protoplanet (initial distance equal to 100).

Chapter 3

Results

3.1 Single planet results

Figures 3.1-3.8 show the evolution with time of the orbital parameters for all single-planet models. The semi-major axis a as a function of time is shown in the top rectangle of each figure; the angular momentum of the protoplanet per unit mass l_z, the abscissa coordinate X_p and the eccentricity e are shown in the following rectangles, respectively. The coordinate X_p is plotted to distinguish each orbit and to allow the counting of the total number of orbits in the simulations. Each figure includes the results from two models, with (models with labels "b" and "d") and without (models "a" and "c") the pseudo-atmosphere. The main feature that emerges from the sub-Keplerian models is a downward migration of the protoplanet, whose speed is strongly dependent on the planet mass. Earth-like planets migrate in a few orbits, especially in the $j = 18$ case, while for the Jupiter-like planets, an extrapolation of the results (which are limited to 20-30 orbits), suggests that a few thousands orbits are necessary to move the planets towards the central star. Of course, the above suggested extrapolation would require a linear behaviour of the semi-major axis (or the specific angular momentum of the planet) with respect to time. But the results obtained for the less massive planet suggest that the migration rate asymptotically

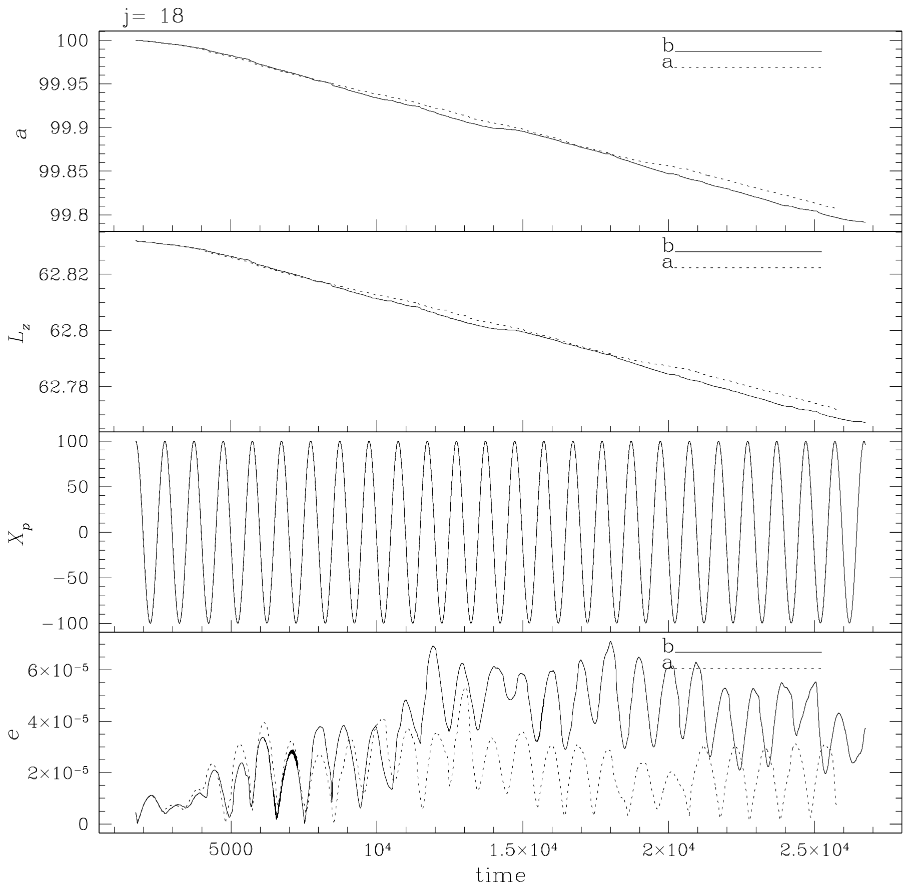

Figure 3.1: Orbital parameters evolution for models 18a and 18b. The semi-major axis a, the specific angular momentum l_z, the x coordinate of the protoplanet and the eccentricity e are reported, as a function of time. The dotted and continuum graphs are for the two reported data sets, with and without the protoplanet pseudo-atmosphere.

decreases for all the three values of the sub-Keplerian angular momentum of the injected particles. All the sub-Keplerian models with the Jovian planet lack the "classical" gap opening around the planet. This is not considered a problem, since the type II migration mechanism, with the planet blocked inside the induced density gap, was developed in the framework of a Keplerian gas distribution in the accretion disc and within a viscosity based fluid model. Therefore, the migration mechanism suggested within the current

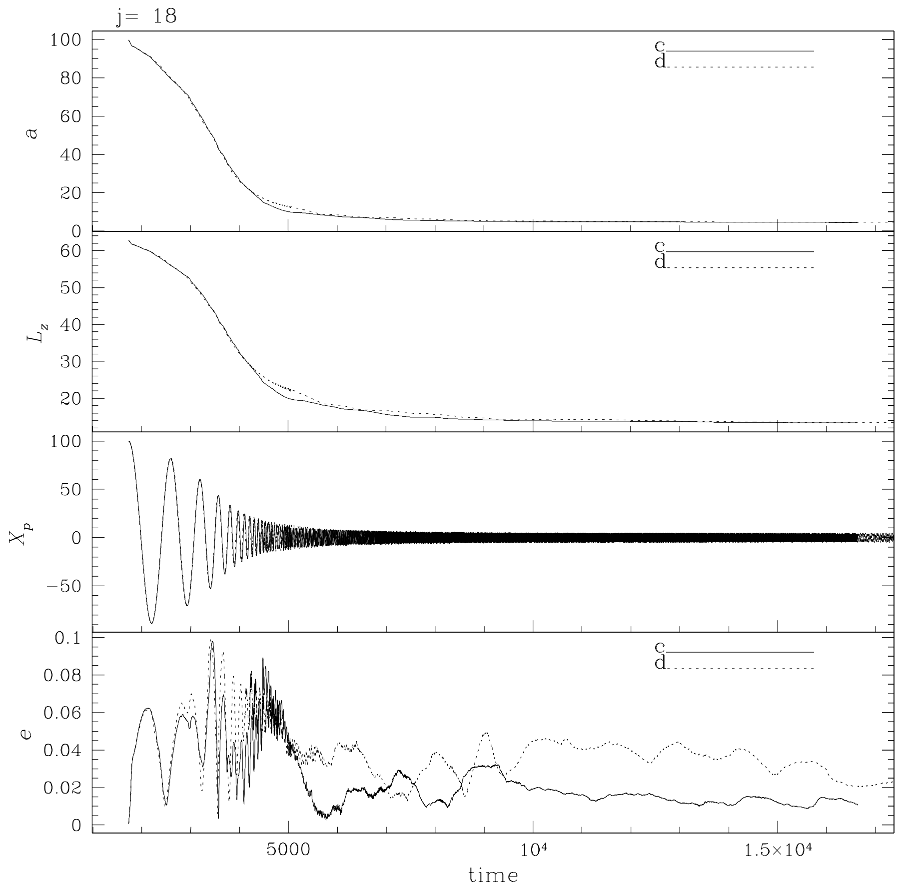

Figure 3.2: Orbital parameters evolution for models 18c and 18d. See the caption in fig. 3.1 for a detailed description.

model cannot be directly associated to the classical type I - type II distinction.

For the Keplerian models, fig. 3.7 shows that the Jupiter-like planet migration slowly proceeds outwards, despite the development of a density gap soon after the introduction of the planet in the initially totally Keplerian gas distribution (fig. 3.9), while the Earth-like planet (fig. 3.8) migrates downward, with a slower rate when compared to that of sub-Keplerian discs. We have in fact 0.6% variation in a in about 30 orbits, while, with the same number of orbits, the sub-Keplerian discs show a $\sim$ 90%; 80%; 50% de-

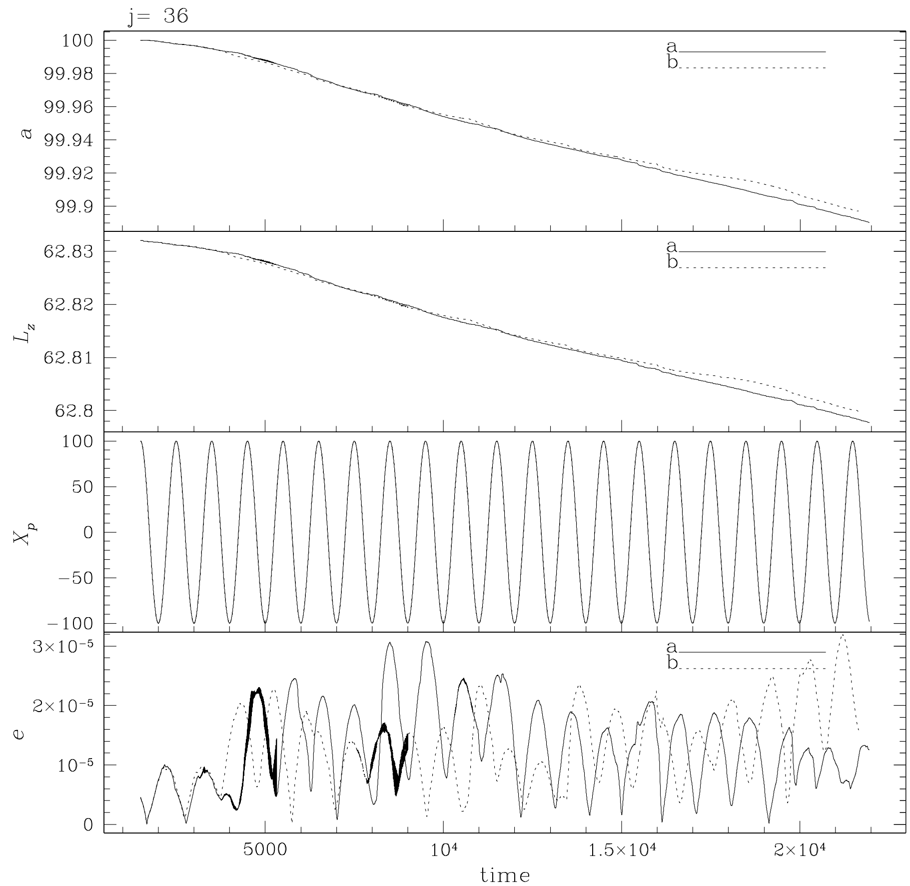

Figure 3.3: Orbital parameters evolution for models 36a and 36b. See fig. 3.1 caption for description.

crease of the planet semi-major axis, for $j_z =$ 18; 36; 54 respectively.

As far as the influence of the pseudo-atmosphere is concerned, the difference between the results obtained with and without this model structure is in the order of $\sim 10^{-2}\%$ with the Jovian protoplanet and of $\sim 1 - 4\%$ with the Terrestrial protoplanet. In most cases we have an initial faster migration rate with the pseudo-atmosphere, but the situation is inverted after a few protoplanet's orbits. This is clearer in models with a Terrestrial protoplanet for which the migration rate is much faster in all models.

A significant difference is registered between the $54c$ and $54d$ models, where

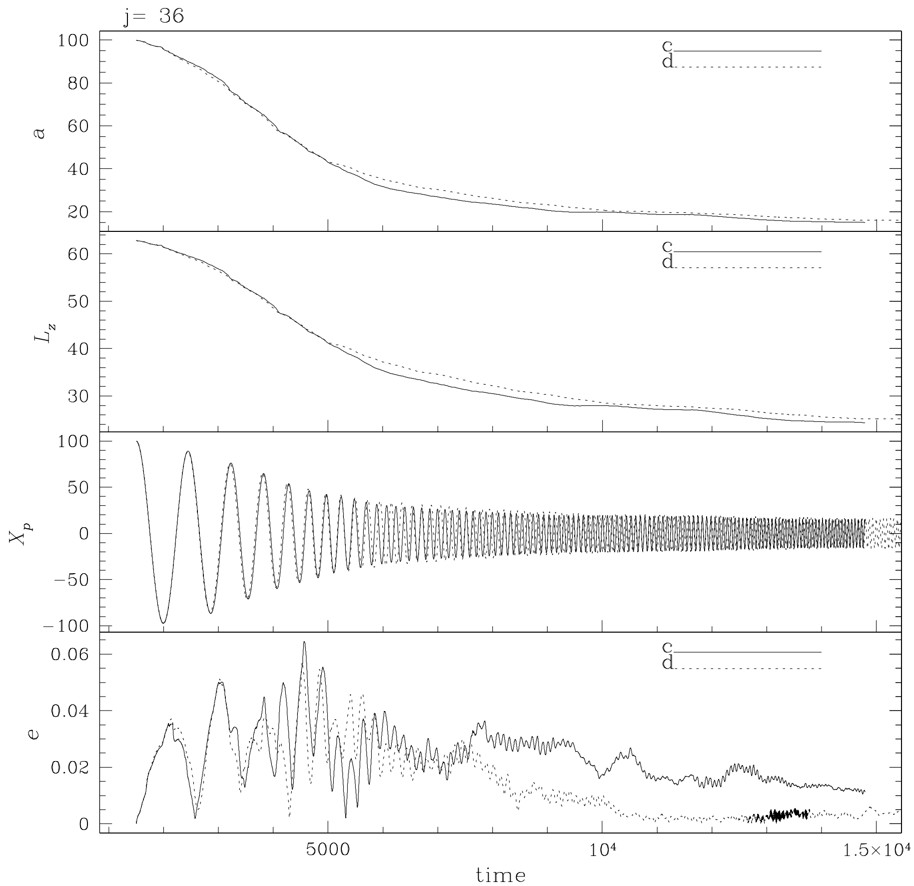

Figure 3.4: Orbital parameters evolution for models 36c and 36d. See the caption in fig. 3.1 for a detailed description.

a $10-15\%$ difference is obtained in the semi-major axis a in advanced migration phases. The model without the pseudo-atmosphere ($54c$) suffers the fastest migration rate at some point.

3.1.1 Angular momentum analytical approximation

In order to draw a semi-analytic behaviour in the orbital parameters time evolution of the planets, best-fittings have been computed for the specific angular momentum of the protoplanet l_z (fig. 3.10-3.13). This gives an estimate of the time derivative and of the decrease lifetime of the angular

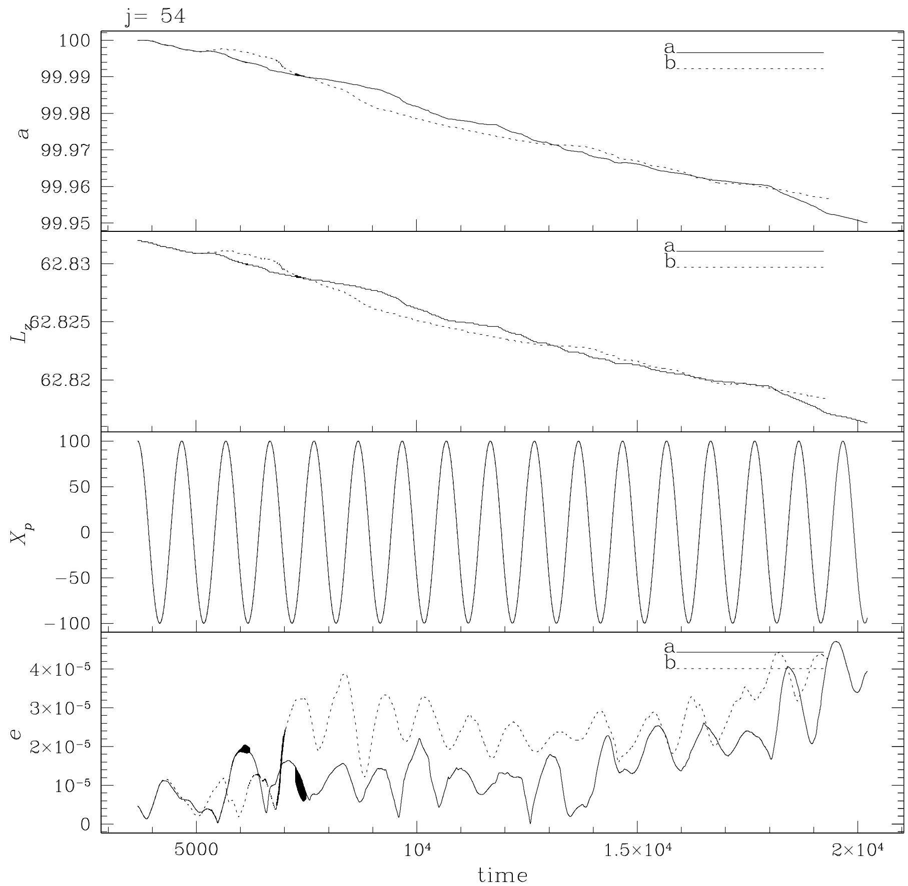

Figure 3.5: Orbital parameters evolution for models 54a and 54b. See the caption in fig. 3.1 for a detailed description.

momentum of each protoplanet. Both linear and exponential fittings were used, according to the following schemes:

$$l_z = a * exp(b \cdot t) + c * exp(d \cdot t) + e \tag{3.1}$$

$$l_z = at + b \tag{3.2}$$

Tables 3.1 and 3.2 report the best-fitting parameters obtained for the various models.

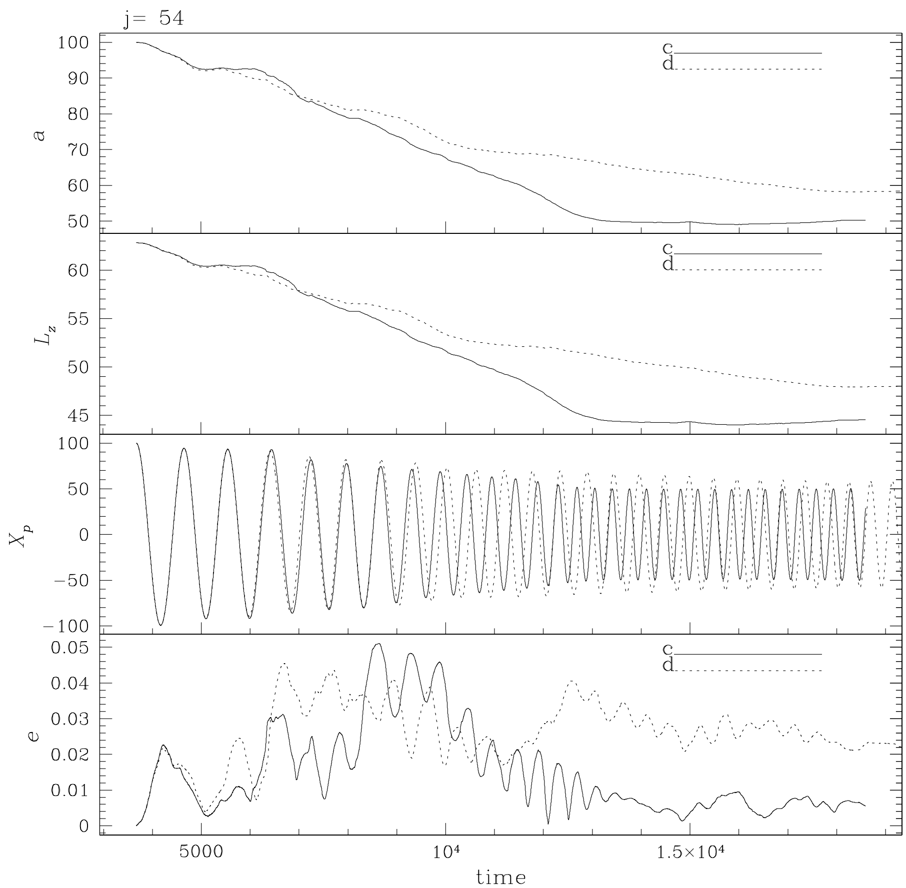

Figure 3.6: Orbital parameters evolution for models 54c and 54d. See the caption in fig. 3.1 for a detailed description.

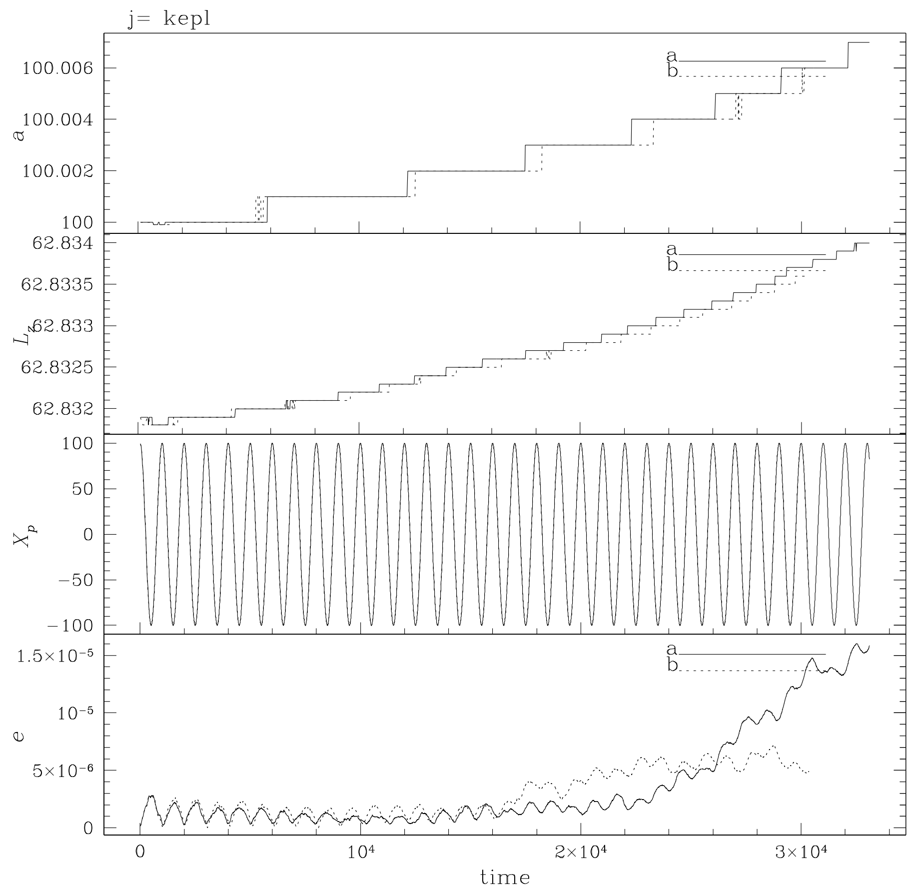

Figure 3.7: Orbital parameters evolution for the Keplerian models and the Jovian planet. See the caption in fig. 3.1 for a detailed description.

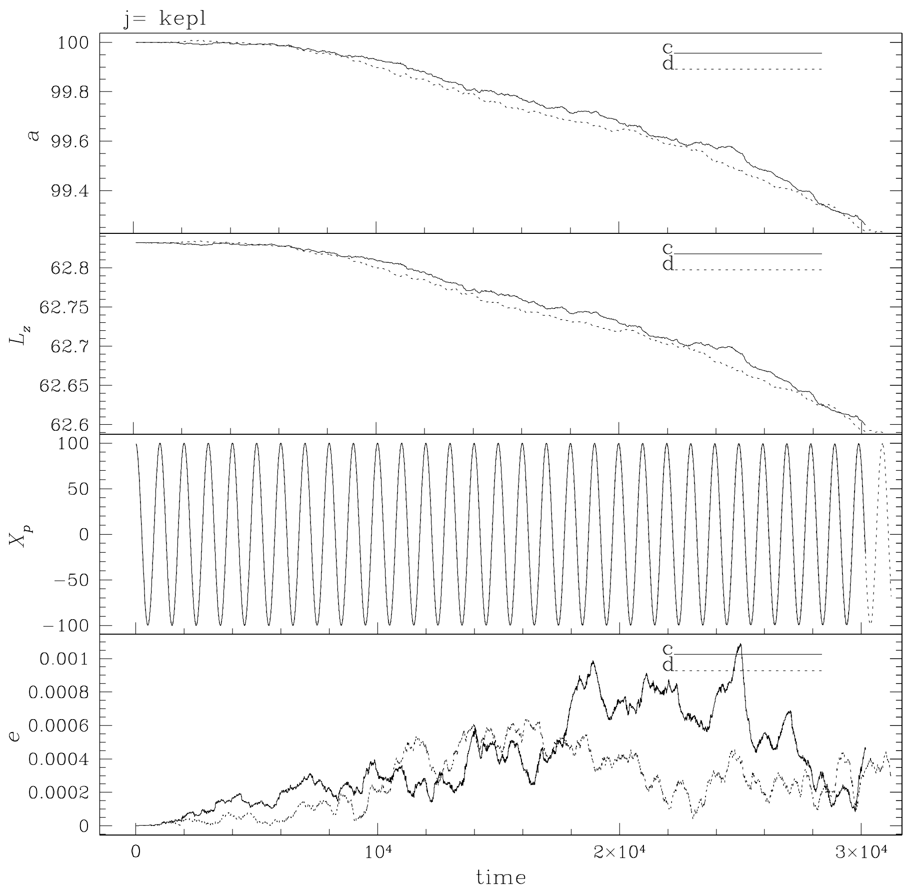

Figure 3.8: Orbital parameters evolution for the Keplerian models and the Earth-like planet. See the caption in fig. 3.1 for a detailed description.

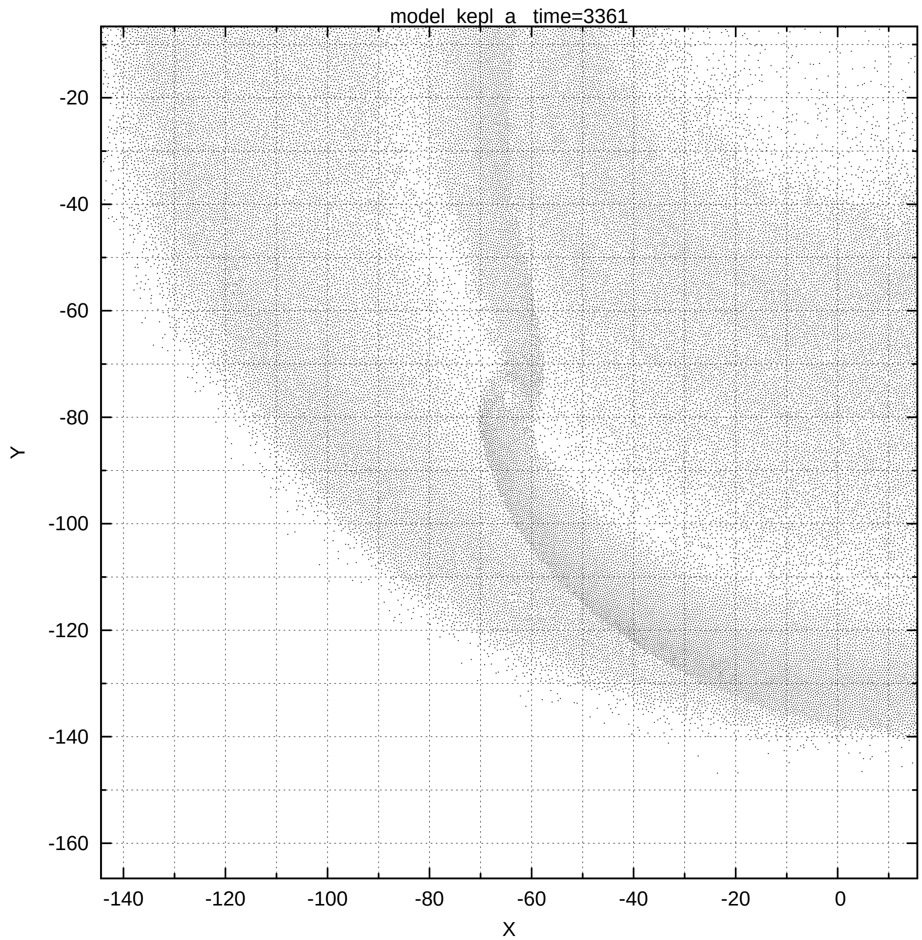

Figure 3.9: Distribution of the gas particles around a Jupiter-like protoplanet in the initially Keplerian accretion disc. This snapshot corresponds to a $\Delta t \sim 3300$ after the artificial formation of a purely Keplerian velocity distribution, which corresponds to a bit more than 3 orbits of the protoplanet.

model	a	b	c	d	e	$1/b$ (years)	$1/d$ (years)
18a	62.87	-3.4×10^{-8}	-3.412 $\times 10^{-2}$	1.059×10^{-5}	2.2×10^{-2}	-2.66×10^{4}	8.54×10
18b	-1.054×10^{-3}	7.134×10^{-5}	62.84	-3.994×10^{-8}	0.0	1.27×10	-2.27×10^{4}
18c	138.4	-4.426×10^{-4}	7.672	3.873×10^{-5}	0.0	-2.04	2.34×10
18d	133.1	-4.547×10^{-4}	10.12	1.822×10^{-5}	0.0	-1.99	4.97×10
36a	62.84	-3.02×10^{-8}	1.228×10^{-4}	1.519×10^{-4}	-4.0×10^{-3}	-3.00×10^{4}	5.96
36b	62.83	-3.209×10^{-8}	1.538×10^{-3}	8.522×10^{-5}	5.0×10^{-3}	-2.82×10^{4}	1.06×10
36c	77.65	-1.842×10^{-4}	7.86	6.437×10^{-5}	0.0	-4.91	1.41×10
36d	63.92	-2.191×10^{-4}	20.37	7.021×10^{-6}	0.0	-4.13	1.29×10^{2}
54a	2.84	-1.557×10^{-8}	7.47×10^{-6}	2.087×10^{-4}	-4.0×10^{-3}	-5.81×10^{4}	4.33
54b	0.1758	-1.734×10^{-5}	62.66	2.504×10^{-8}	2.2×10^{-3}	-5.22×10	3.61×10^{4}
54c	-	-	-	-	-	-	-
54d	56.29	-4.93×10^{-5}	14.5	3.032×10^{-5}	0.0	-1.84×10	2.98×10
kepl_a	62.83	5.484×10^{-10}	6.264×10^{-5}	8.953×10^{-5}	1.7×10^{-3}	1.65×10^{6}	1.01×10
kepl_b	62.83	4.825×10^{-10}	1.375×10^{-4}	6.635×10^{-5}	1.65×10^{-3}	1.87×10^{6}	1.36×10
kepl_c	65.74	-6.256×10^{-7}	-2.903	-1.407×10^{-5}	0.0	-1.45×10^{3}	-6.43×10
kepl_d	-1.982	1.227×10^{-5}	64.83	3.28×10^{-7}	0.0	7.37×10	2.76×10^{3}

Table 3.1: Exponential best-fitting parameters for the specific angular momentum l_z time evolution (eq. 3.1). A rough estimate of migration times is given by the inverse of the two parameters b and d, dimensioned values in *years* are given in 7th and 8th columns, calculated under the hypothesis of 1 $M_\odot$ star with a radius of $\sim 2\ R_\odot$.

model	a	b	τ (adim)	τ (years)
18a	-2.555×10^{-6}	62.838	2.46×10^{7}	2.23×10^{4}
18b	-2.717×10^{-6}	62.84	2.31×10^{7}	2.09×10^{4}
18c	-1.48685×10^{-2}	93.2653	4.23×10^{3}	3.83
18d	-141492×10^{-2}	90.8171	4.44×10^{3}	4.02
36a	-1.762×10^{-6}	62.836	3.57×10^{7}	3.23×10^{4}
36b	-1.638×10^{-6}	62.836	3.84×10^{7}	3.47×10^{4}
36c	-6.49898×10^{-3}	74.9447	9.67×10^{3}	8.75
36d	-6.37015×10^{-3}	74.307	9.86×10^{3}	8.92
54a	-9.533×10^{-7}	62.836	6.59×10^{7}	5.96×10^{4}
54b	-9.36912×10^{-7}	62.8356	6.71×10^{7}	6.07×10^{4}
54c	-1.90167×10^{-3}	70.8222	3.30×10^{4}	29.9
54d	-1.42529×10^{-3}	68.0032	4.41×10^{4}	39.9

Table 3.2: Linear best-fitting parameters for the specific angular momentum l_z time evolution (eq. 3.2). For some cases, the linear fitting is calculated over a limited time interval, during which the angular momentum evolution is linear. The linear fittings are not present for the Keplerian models since there is no time interval during which the evolution of the angular momentum is linear. Migration times estimated with the formula $l_z/\dot{l}_z$ are reported in the last two columns: in the fourth column the dimensionless time is reported, while in the last column the same time is converted in *years* by choosing 1 $M_\odot$ and 2 $R_\odot$ as physical reference units.

In table 3.1 the last two columns give the inverse values of the parameters b and d, and they have been dimensioned in *years* by choosing 1 $M_\odot$ and 2 $R_\odot$ as reference units. Of the two time-scales estimated in this way, the most important is the one with the corresponding highest "multiplying factor for the exponential" (a or c). For Jupiter-like planets these estimates must be taken with some care, as the simulations did not go enough far in time to have a clear path of the migration process. Therefore, the migration timetable of these models could be different than what expected from extrapolations.

In table 3.2 the 4th column gives a dimensionless migration time, evaluated as $l_z/\dot{l_z}$, and the last column gives the same time converted in years by choosing the same reference units as in table 3.1.

For models a and b (Jovian planet) a linear fitting already gives a good

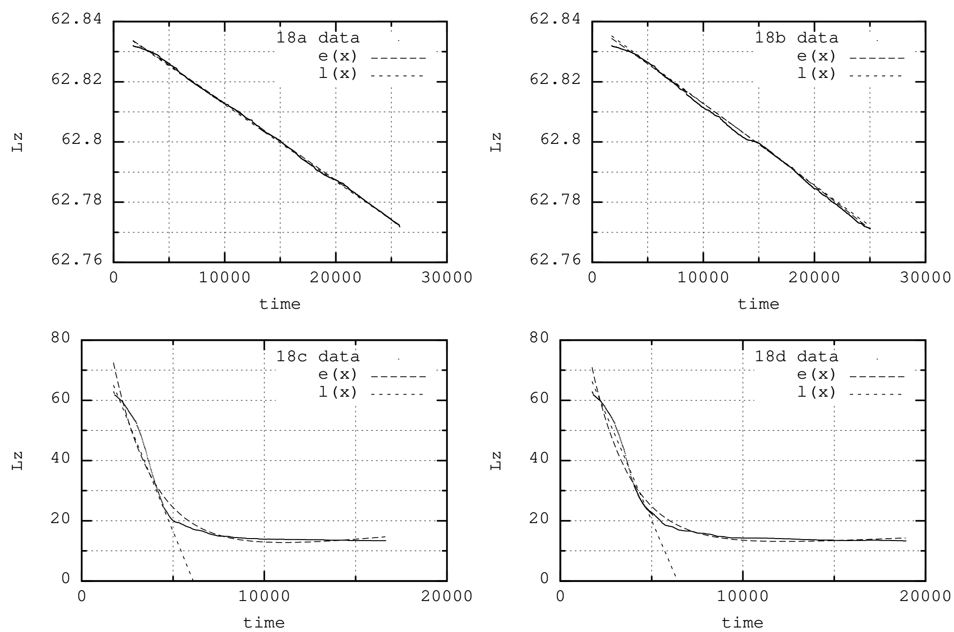

Figure 3.10: Data and exponential best-fittings for the angular momentum l_z of the protoplanet in $j = 18$ models

description of the angular momentum evolution of the planet, but an exponential fitting has also been performed because, on a longer time-scale (a few thousands orbits), the curve showing l_z as a function of time could resemble that of the c and d models. We are therefore able to analyse the different migration lifetimes through comparable parameters (exponential lifetime or linear constant derivative).

For some of the c and d models, the behaviour is initially linear and it becomes more exponential once the protoplanet reaches a position closer to the star. In these cases, the linear fitting has been done for a limited time interval during which the evolution does not show a significant migration

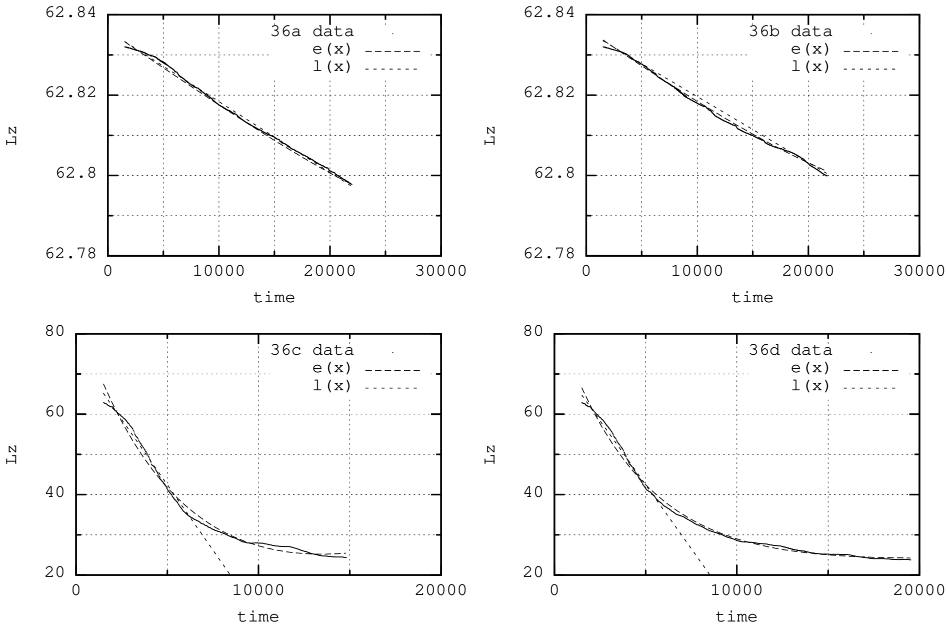

Figure 3.11: Data and exponential best-fitting for the angular momentum in $j = 36$ models

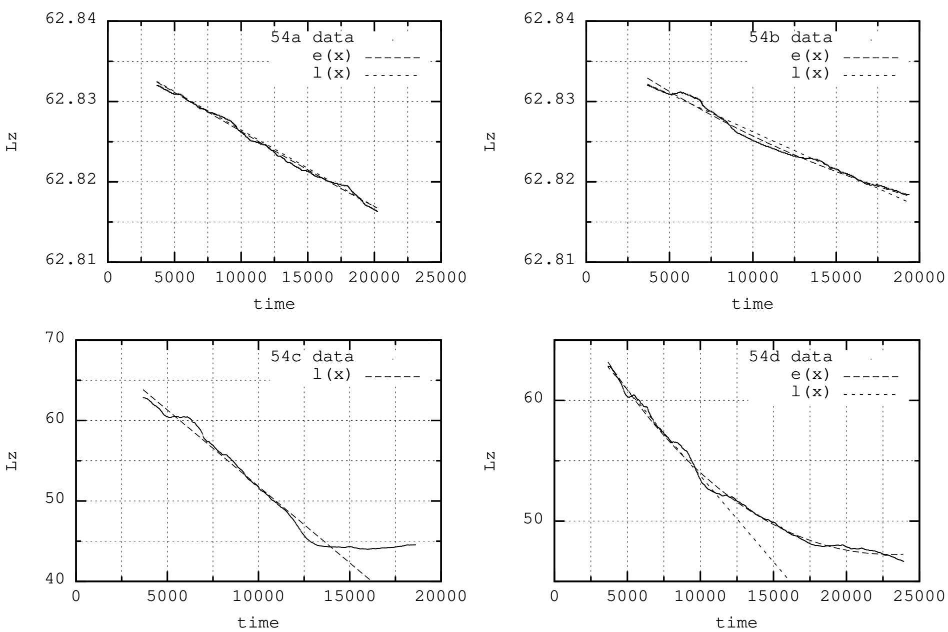

Figure 3.12: Data and exponential best-fittings for the angular momentum l_z of the protoplanet in $j = 54$ models

rate variation. A peculiar case is the $54c$ model where an initial linear behaviour with negative derivative is followed by a nearly complete migration

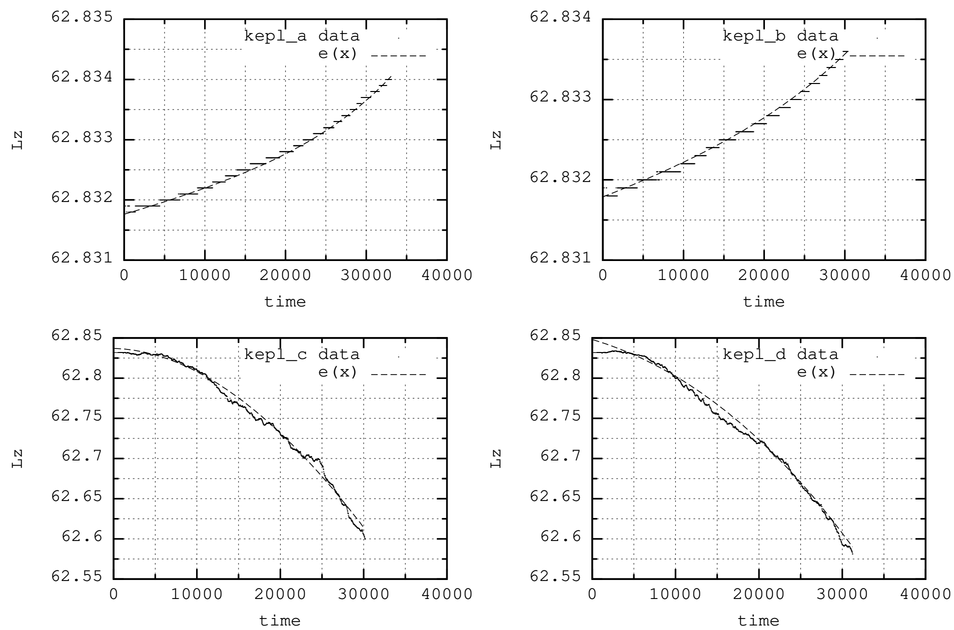

Figure 3.13: Data and exponential best-fittings for the angular momentum l_z of the protoplanet in Keplerian models

stop. The exponential fitting has not been evaluated for this model.

3.1.2 Shock waves

Propagation of waves coming from the central zone of the disc has been observed, at least for the $j = 18$ and $j = 36$ models. Some snapshots showing this phenomenon are plotted in fig. 3.14 and 3.15. The same is not clearly observed in the other models, the cause being probably the higher angular momentum of particles. A strong sub-Keplerian condition for injected particles makes them rapidly fall towards the centrifugal barrier, and the subsequent bouncing-back could be at the origin of these waves. Details on this propagation of shock waves in systems with a central accreting object was described by Lanzafame et al. (2008) and references therein. A proper combination of sub-Keplerian gas flow and viscosity parameter values can create a complex shock structure with nearly periodical radial motions of the shock front. Periods of quiet piling up of particles near and below the

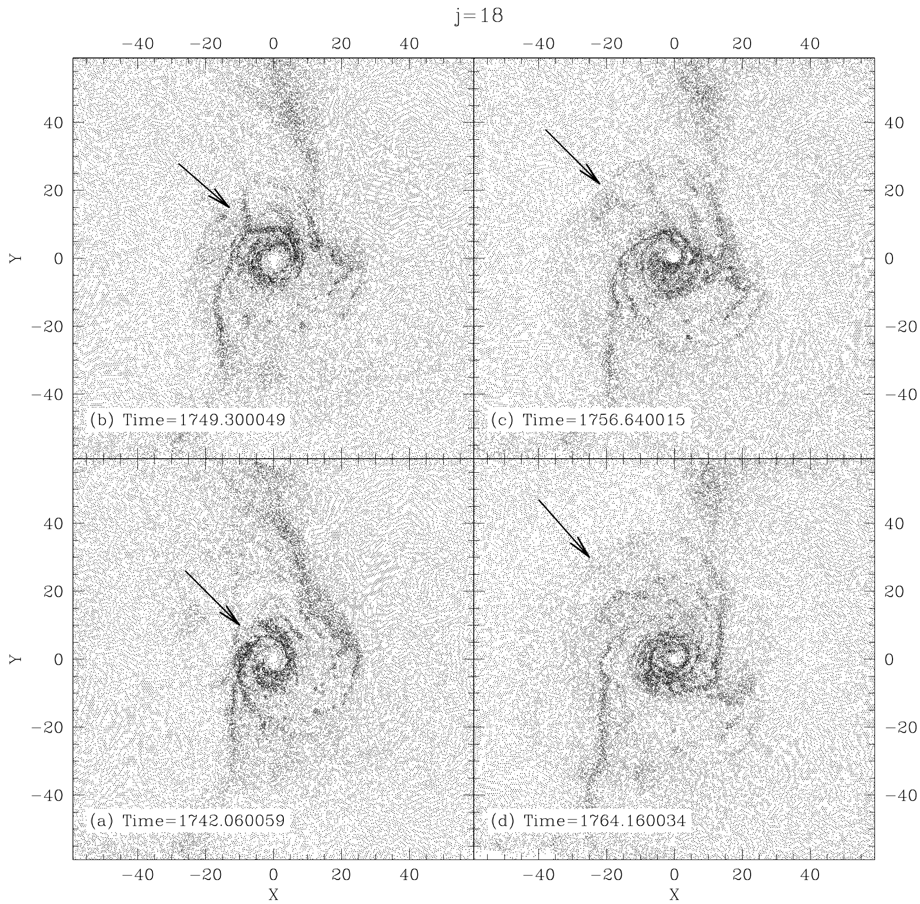

Figure 3.14: Wave propagation in the $j = 18$ accretion disc. The four snapshots are ordered according to increasing time, starting from the bottom-left square in clock-wise order. The arrows indicate the position of a shock front.

centrifugal barrier are followed by the development of a shock front propagating outwards. In low or no viscosity regimes, the position of the shock front is generally closer to the central accreting object.

3.2 Two planets

The results obtained with the models including two protoplanets are shown in figures 3.16-3.27. Each figure includes four graphs where, from the top rectangle to the bottom one, the semi-major axis a, the orbital period P,

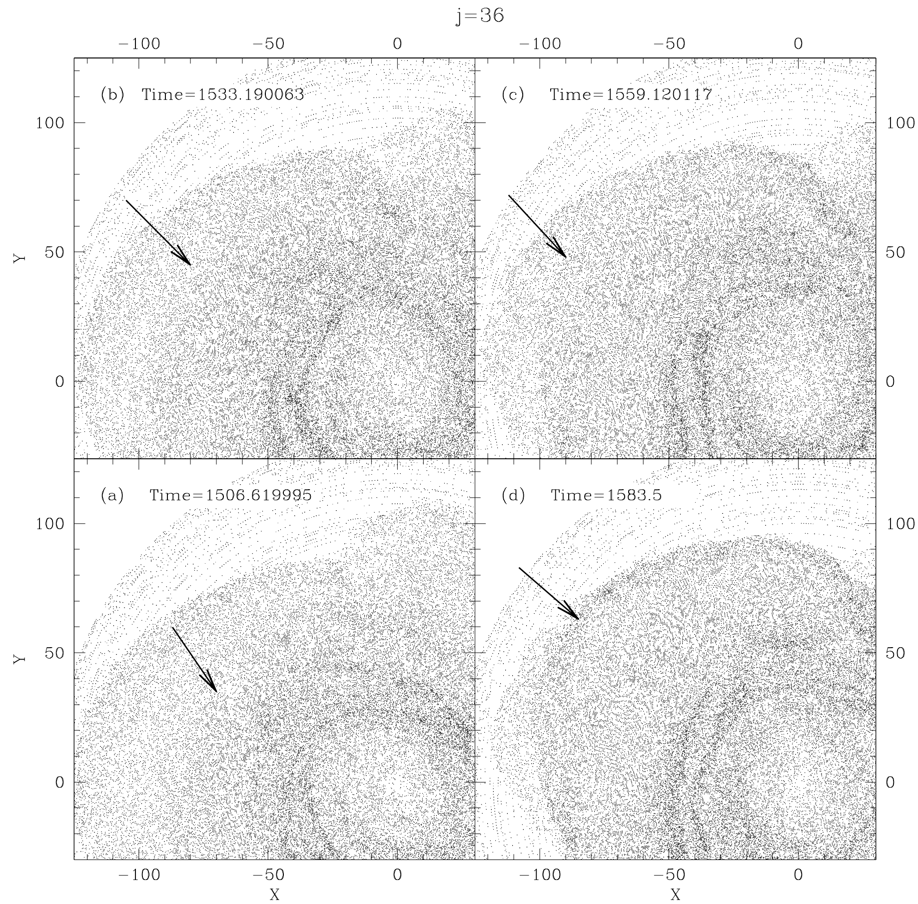

Figure 3.15: Wave propagation in the $j = 36$ accretion disc. The four snapshots are ordered according to increasing time, starting from the bottom-left square in clock-wise order. The arrows indicate the position of a shock front.

the eccentricity e and the specific angular momentum l_z are plotted as a function of time.

Each graph shows the orbital parameters evolution of two protoplanets, the external one in red and the internal one in blue. The total number of orbits can be roughly estimated by dividing the total time of the simulation, given in the abscissa, by the value of the orbital period.

The general trend of this second set of data is that all the sub-Keplerian models show orbital decay of both planets, while initially Keplerian mod-

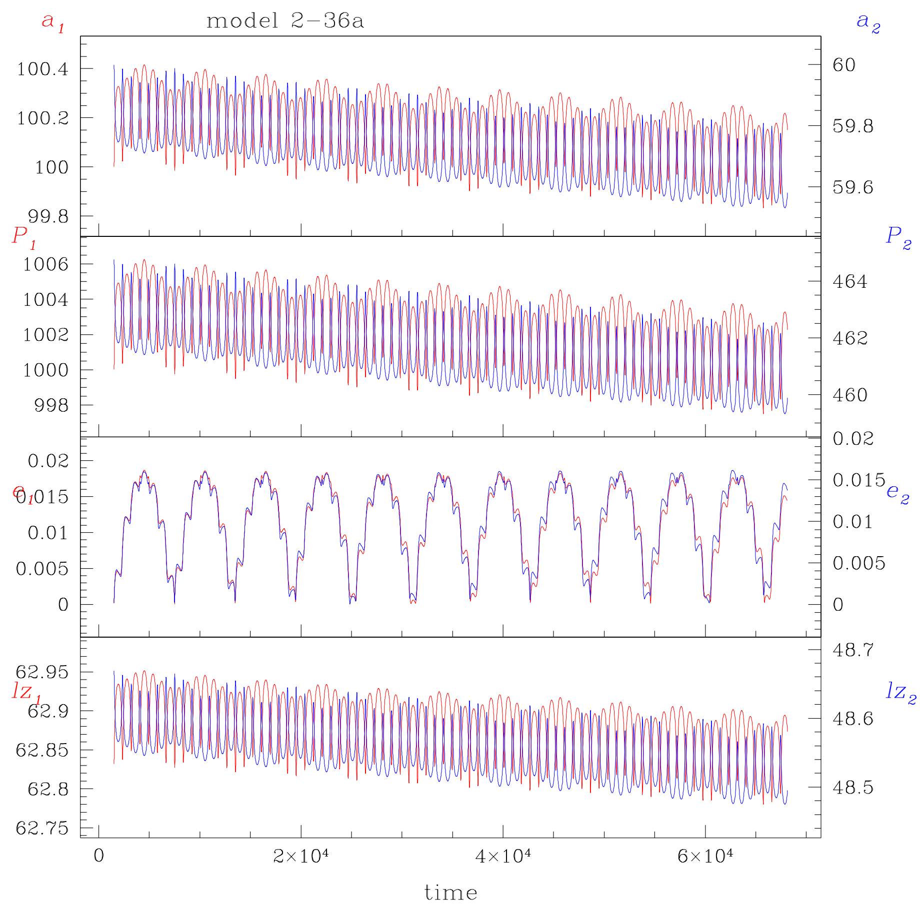

Figure 3.16: Orbital parameters evolution for model 2_36a. The semi-major axis a, the orbital period P, the eccentricity e and specific angular momentum l_z, as a function of time are plotted in the four rectangles. The red and blues graphs are for the external and internal protoplanets respectively.

els show enlarging orbits in some cases. The speed of orbital changes are very different according to protoplanets masses and accretion disc angular momentum. This path is similar to what already observed for single planet models for $j = 36, 54$.

Concerning the specific features related to the two-planets configuration, the main results depend on the two-planets masses combination (Jovian - Jovian, internal Terrestrial - external Jovian, internal Jovian - external Terrestrial, Terrestrial - Terrestrial). The simulations have been running for

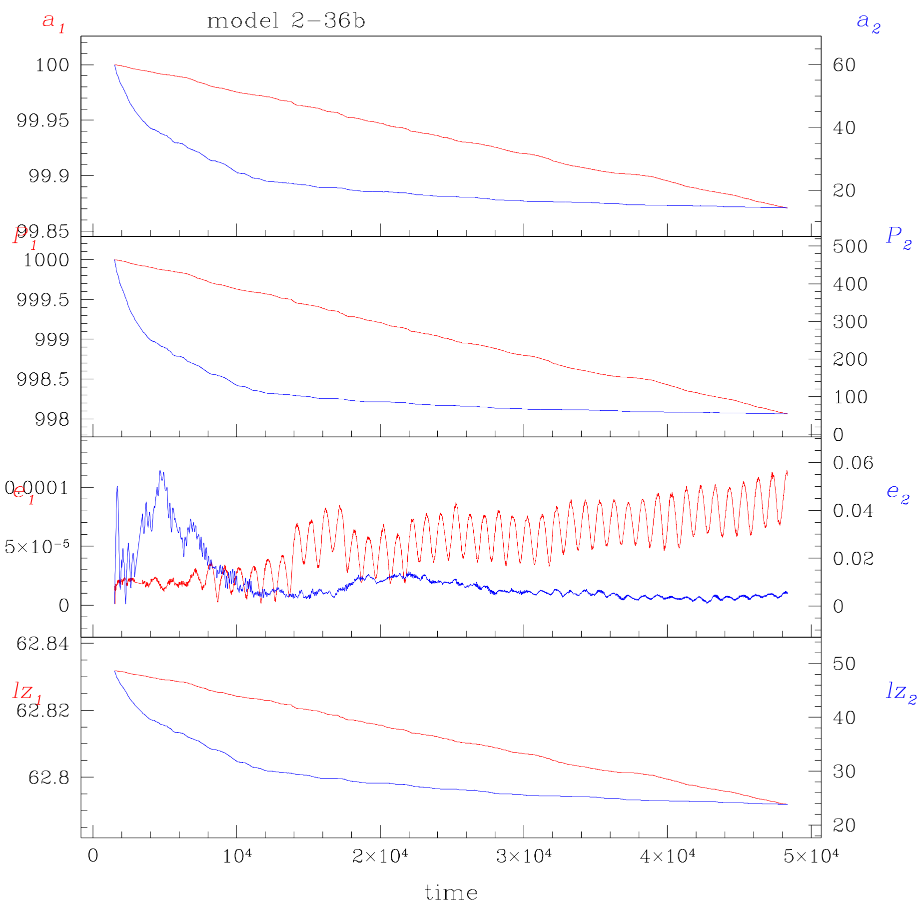

Figure 3.17: Orbital parameters evolution for model 2_36b. See the caption in fig. 3.16 for details.

a time corresponding to about 50-200 protoplanetary orbits. Looking at the models labelled with a (figures 3.16, 3.20), including two Jovian planets, the following main features can be observed:

1. a slow decrease of the semi-major axis;

2. an oscillatory behaviour of both the semi-major axis a and the eccentricity e. These oscillations are characterised by more than one period and "beats" are quite clearly observable in the eccentricity time profile and in the semi-major axis profile;

3. the observed beat period is in the 1350-1400 range, which is in line with

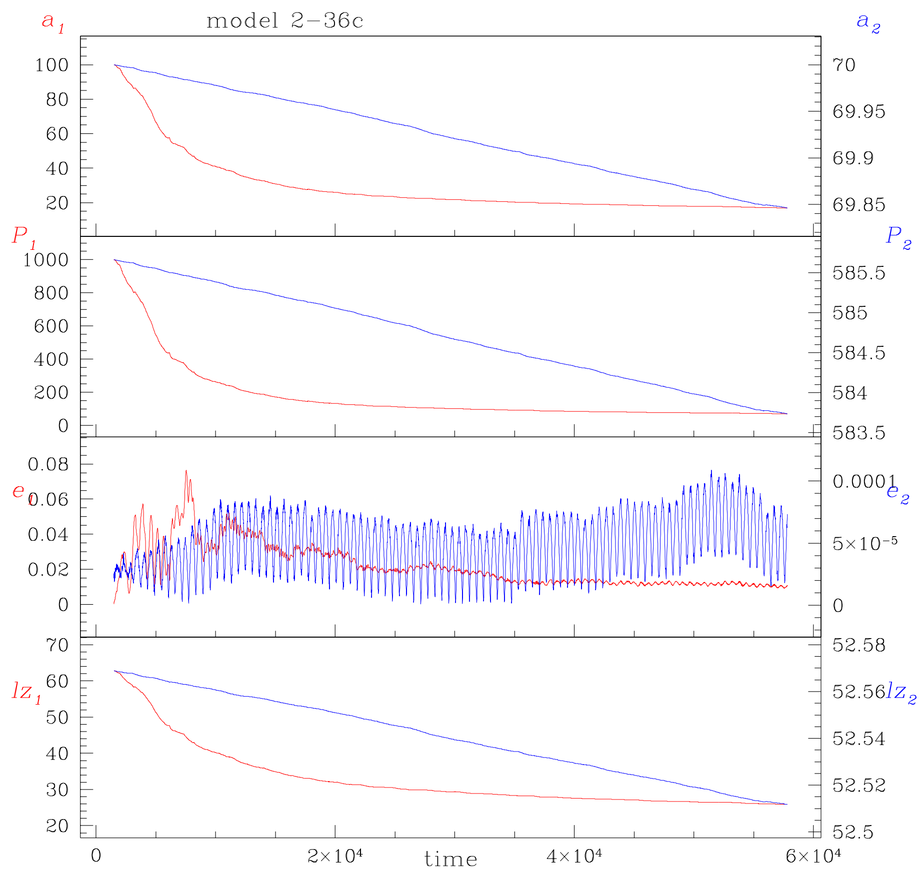

Figure 3.18: Orbital parameters evolution for model 2_36c. See the caption in fig. 3.16 for details.

a beat generated by two periods of 1000 and 585 (the initial periods of the two protoplanets).

In b models (external Jovian - internal Terrestrial, figures 3.17, 3.21) the presence of beats is not evident, probably due to the much weaker gravitational interaction between the two protoplanets. A fast decay of the Terrestrial protoplanet orbit is visible, as observed for single planet models. Similar observations can be addressed to the c models (external Terrestrial - internal Jovian, figures 3.18, 3.22), where the external planet has a rapidly decaying orbit. In both b and c models, the decay paths are similar to what

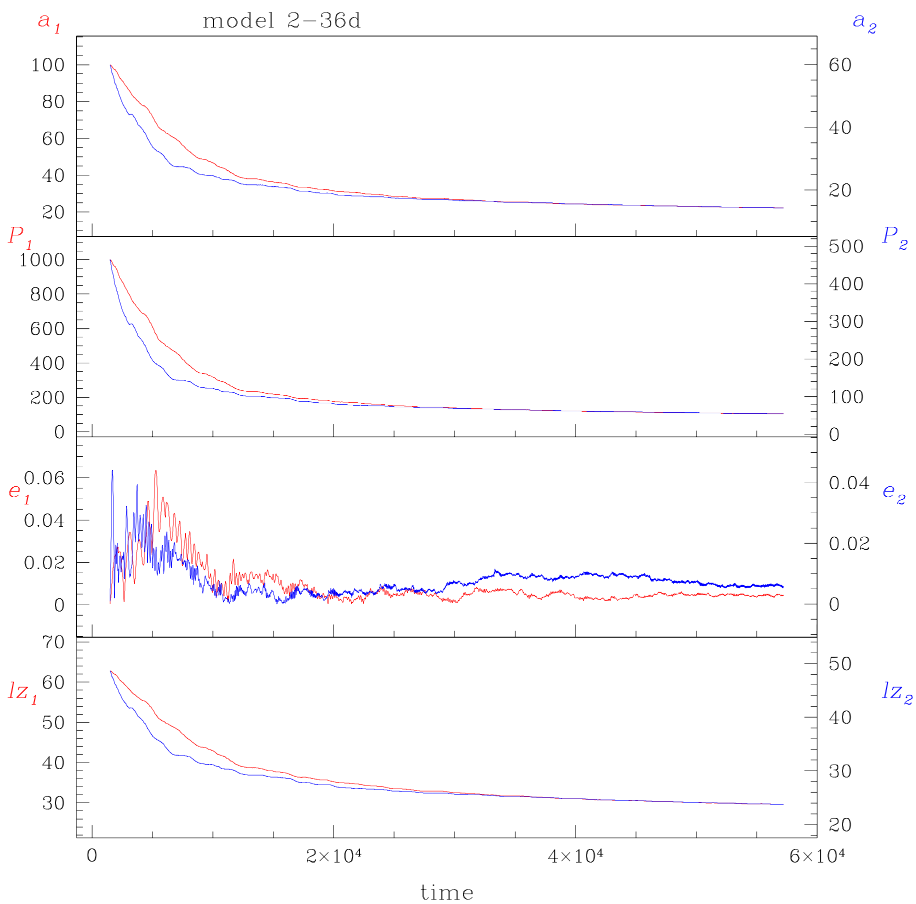

Figure 3.19: Orbital parameters evolution for model 2_36d. See the caption in fig. 3.16 for details.

observed with single planet models, each planet migrates according to its mass. Although an exception can be found for model 2_54c (fig. 3.22), where a sudden change of all the tracked orbital parameters is found at a time of $\sim 2 \times 10^4$. This sudden change clearly happens where the two semi-major axes are very similar, and it is certainly due to a close encounter of the two-planets.

The *d* models (figures 3.19, 3.23), characterised by the weakest planet-planet interaction (two Terrestrial protoplanets), show a rapidly decaying orbit for both planets, as observed in single planet models with Terrestrial mass.

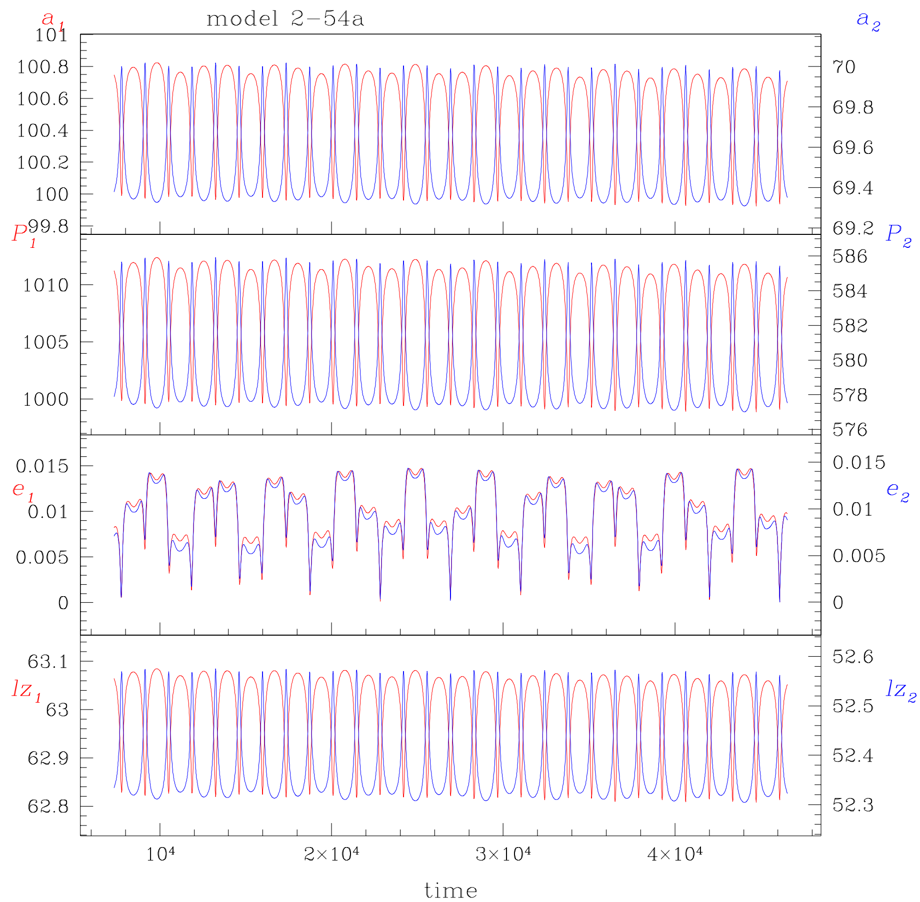

Figure 3.20: Orbital parameters evolution for model 2_54a. See the caption in fig. 3.16 for details.

Concerning the Keplerian models (figures 3.24-3.27), it can be said that:

1. the *a* model with Jovian like protoplanets show oscillations of the orbital parameters, but the migrations of the protoplanets proceeds outward, instead of inward;

2. the *b* and *c* models show oscillations of eccentricity for both planets, but the most evident oscillation involves the Earth-like planet, as expected; initial inward, followed by outward migration is observed for the Terrestrial planet in both models; the Jovian planet follows an outward migration in model *b* and an inward migration in model *c*;

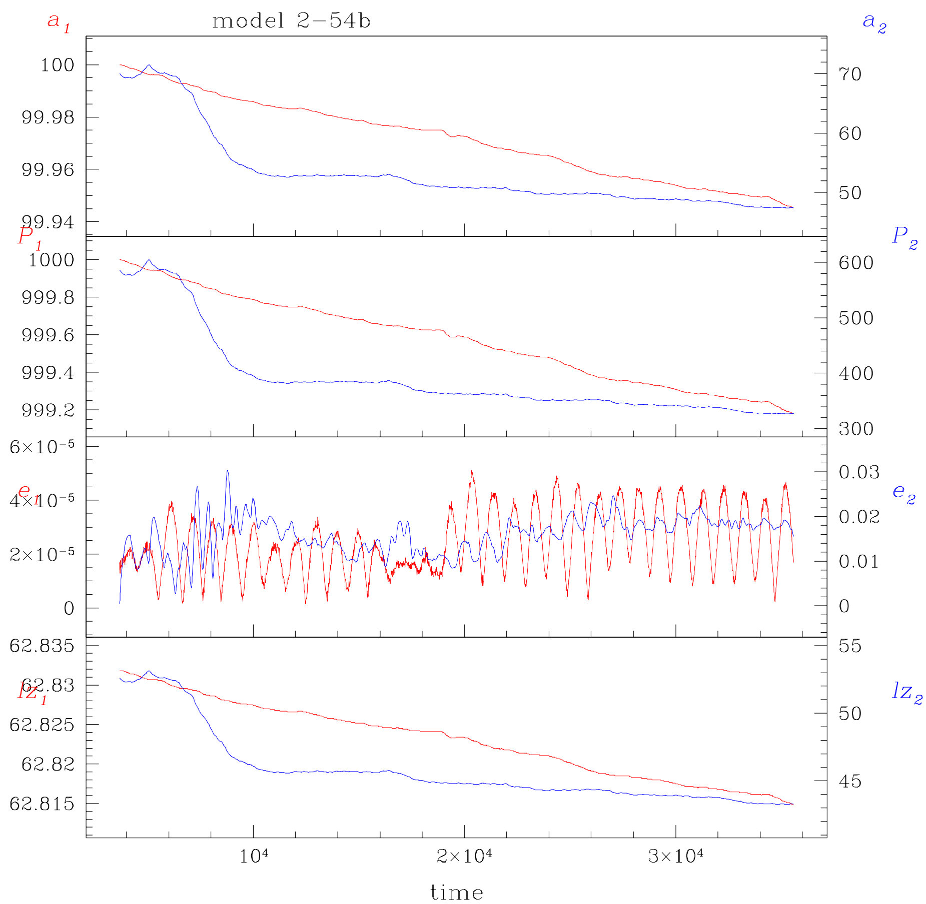

Figure 3.21: Orbital parameters evolution for model 2_54b. See the caption in fig. 3.16 for details.

3. in model *d* (both Terrestrial planets), no evident oscillations or beats are present, and an inward migration is observed, somewhat similar to what observed with single planet model *kepl_c*.

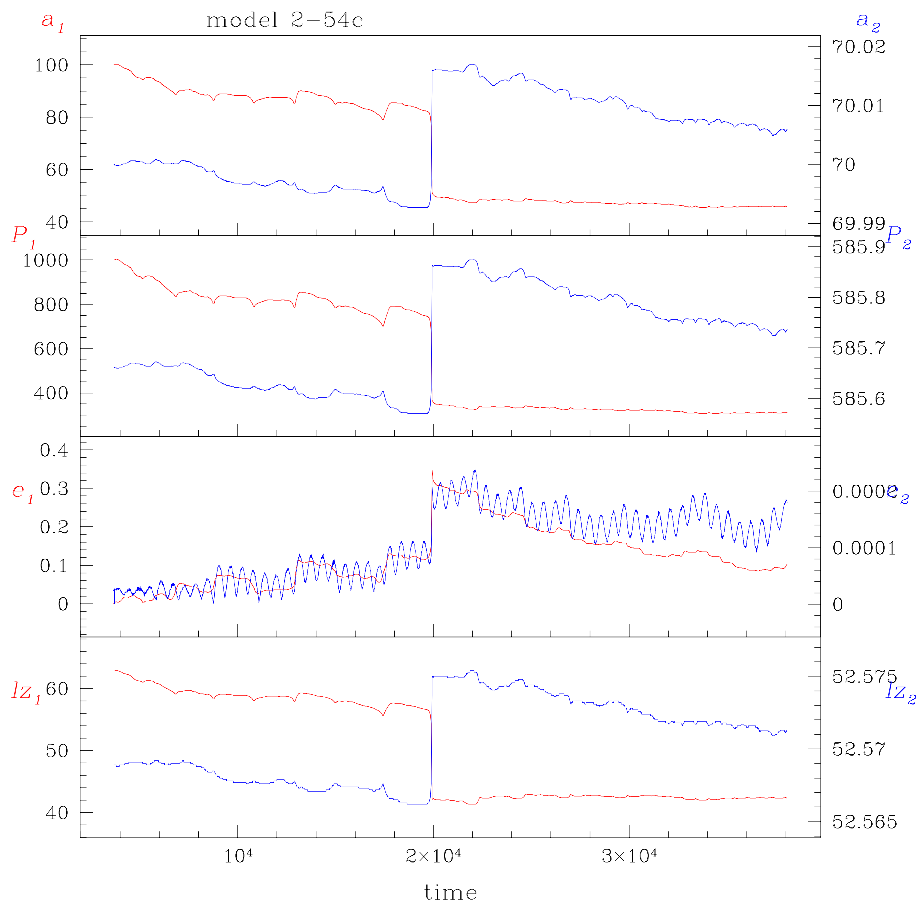

Figure 3.22: Orbital parameters evolution for model 2_54c. See the caption in fig. 3.16 for details.

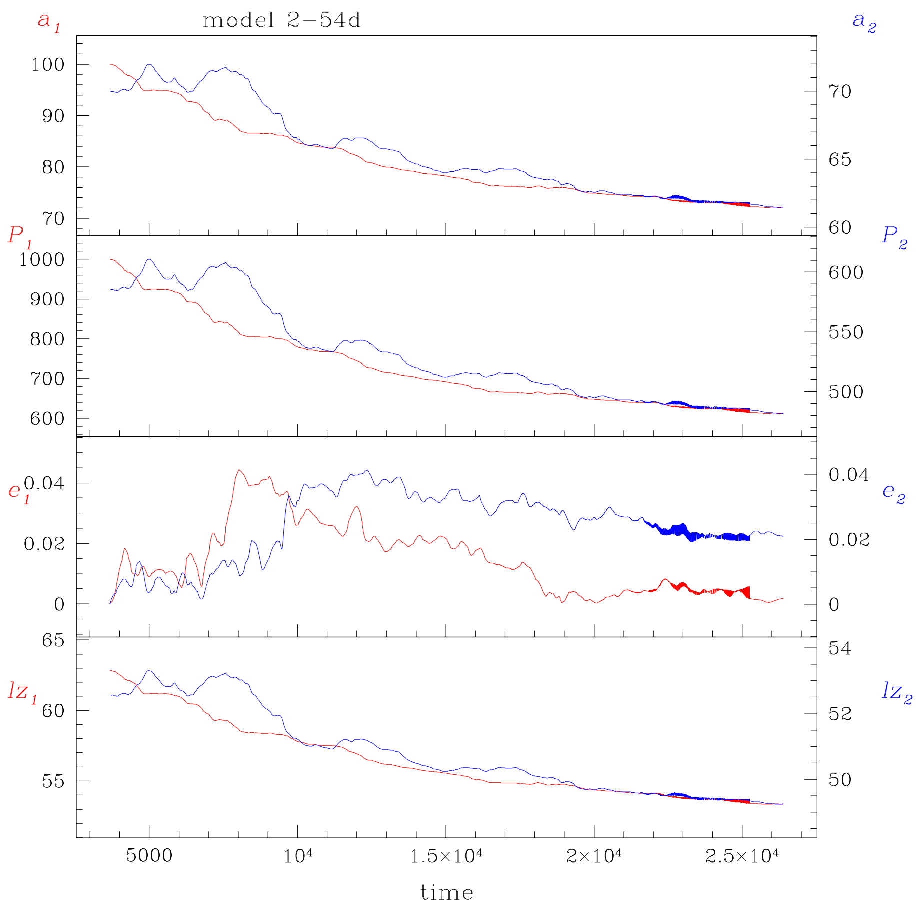

Figure 3.23: Orbital parameters evolution for model 2_54d. See the caption in fig. 3.16 for details.

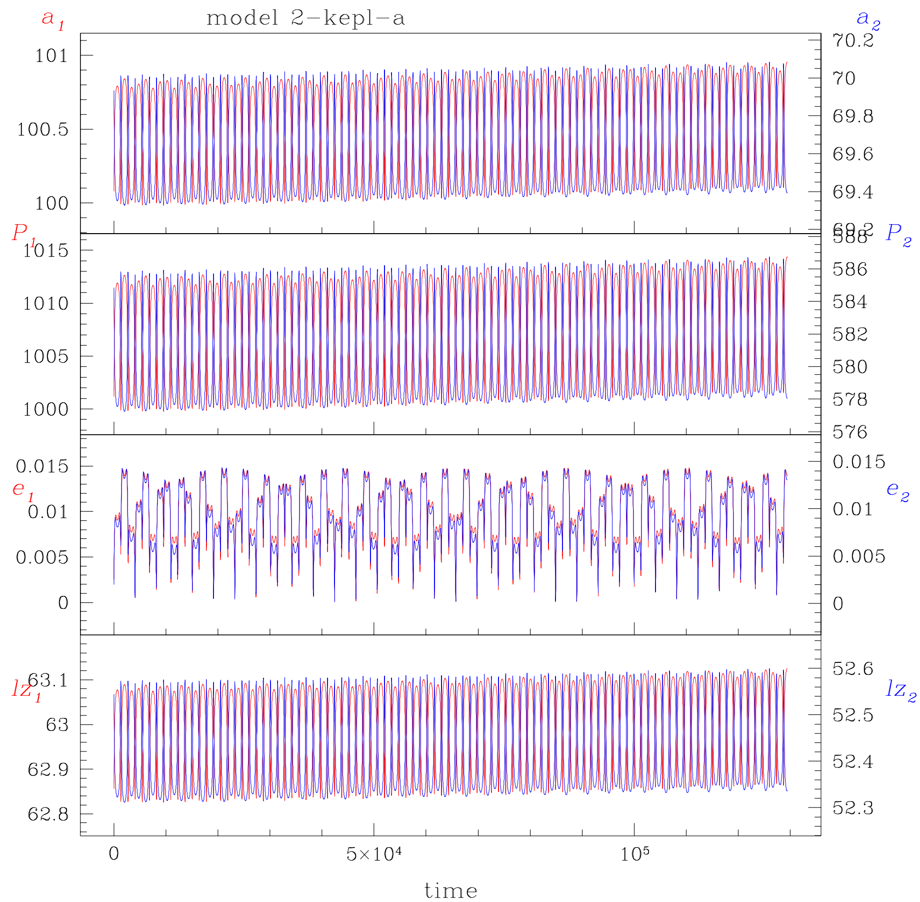

Figure 3.24: Orbital parameters evolution for model 2_kepl_a. See the caption in fig. 3.16 for details.

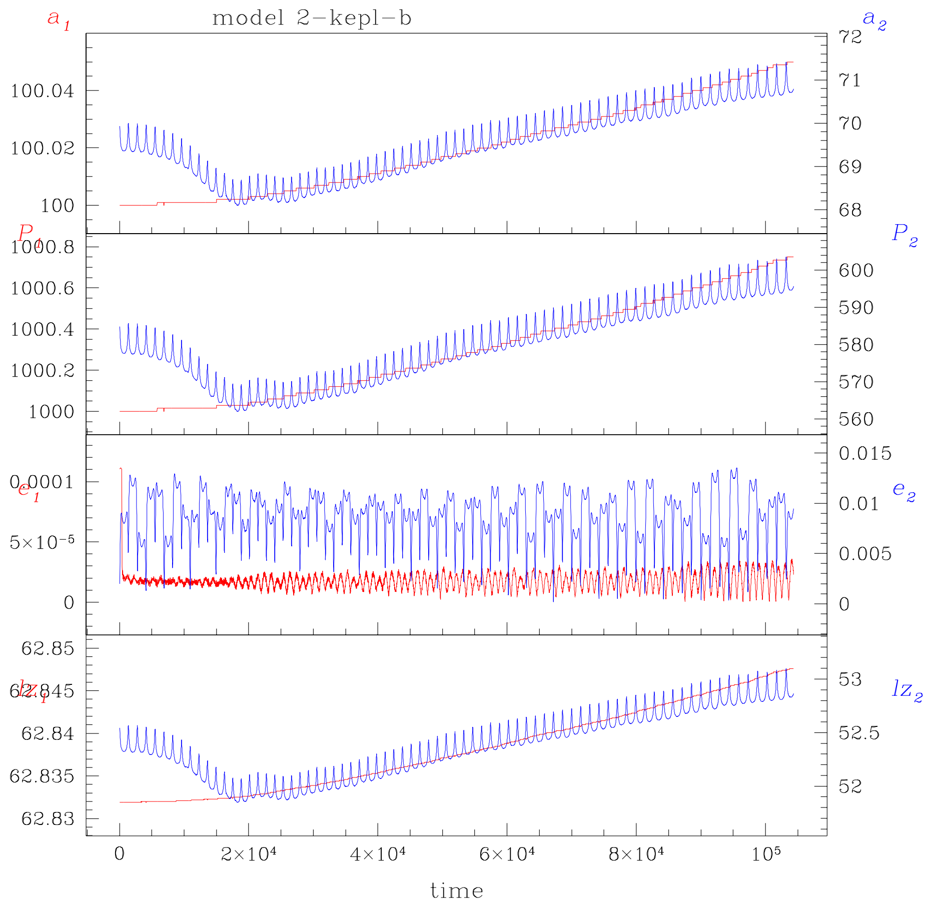

Figure 3.25: Orbital parameters evolution for model 2_kepl_b. See the caption in fig. 3.16 for details.

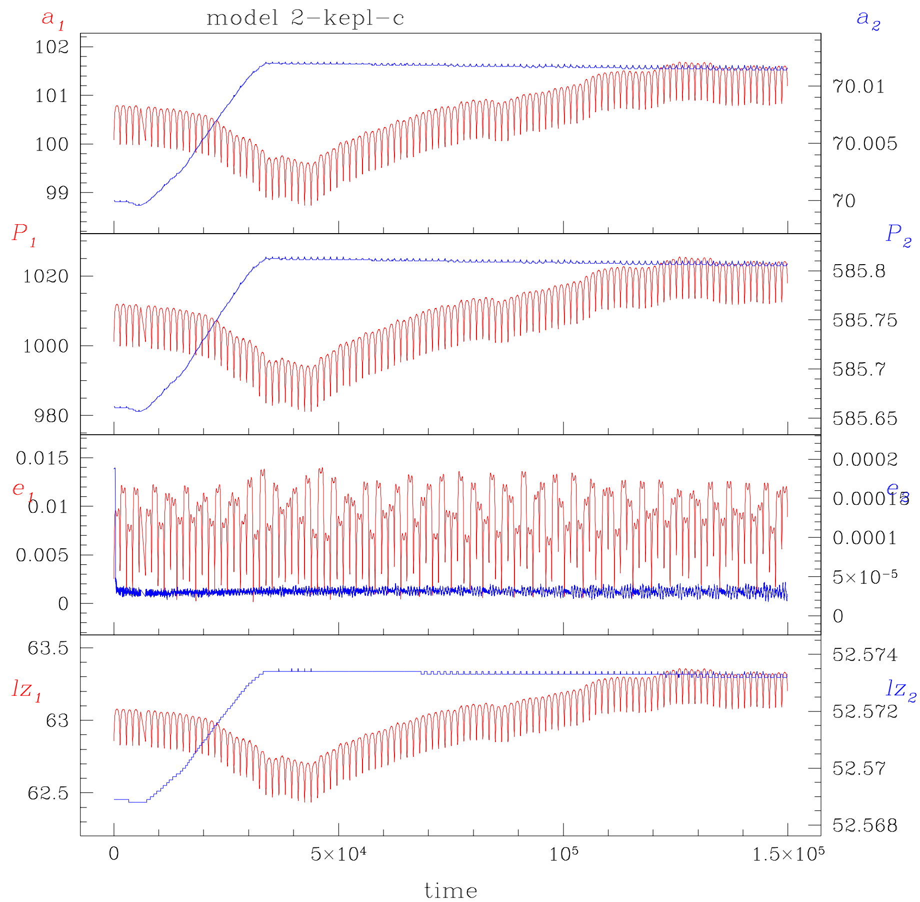

Figure 3.26: Orbital parameters evolution for model 2_kepl_c. See the caption in fig. 3.16 for details.

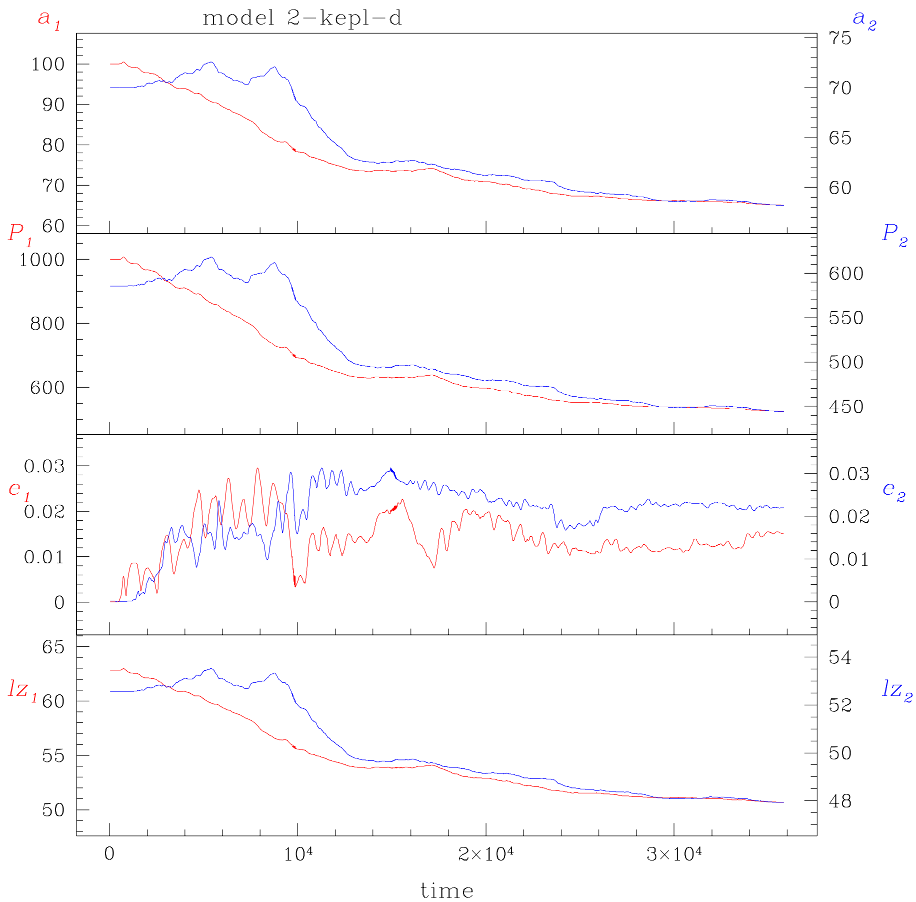

Figure 3.27: Orbital parameters evolution for model 2_kepl_d. See the caption in fig. 3.16 for details.

3.3 Keplerian test

Together with the simulations specified in tables 2.1 and 2.2, a peculiar numerical simulation has been performed in order to test the stability of the Keplerian kinematics. The test is based on the same code used for the other simulations, but without the planet and with an initially totally Keplerian distribution of velocities. The aim of the test is to analyse the survival time of the Keplerian kinematics before consistent radial perturbations comes out. Results are shown in fig. 3.28, where the ratio "radial speed/Keplerian

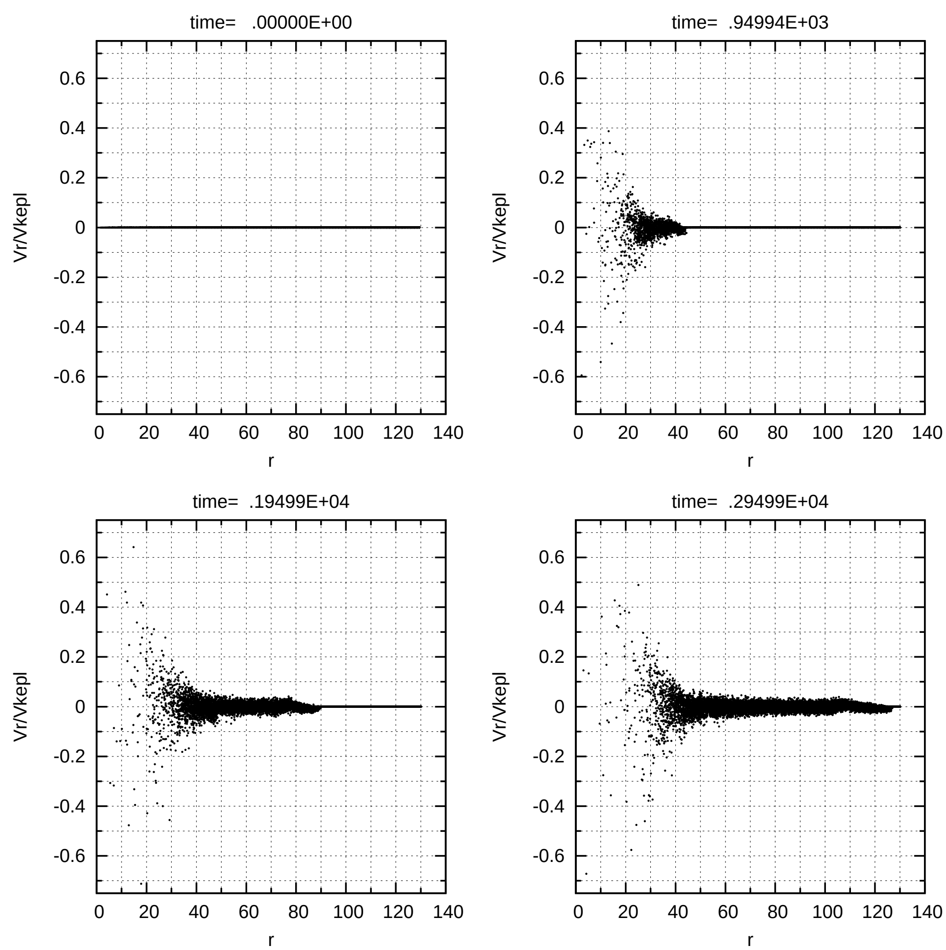

Figure 3.28: Distribution of the ratio "radial speed/Keplerian speed" as a function of radial distance for an initially totally Keplerian model. The four graphs show snapshots obtained at various times, considering that $t = 1000$ is one orbital period at a distance $r = 100$.

speed" is plotted as a function of the radial distance to the central star. Four snapshots are provided at different times, the first at time zero, and the last at $t = 3000$ (corresponding to three Keplerian orbits at $r = 100$). A spontaneous breaking of the initially Keplerian kinematics is observed, due to the contribution of pressure forces and to the collisional nature of the model. Both downward and outward migrating particles are produced, especially in the inner parts of the disc. This results show how useful is the analysis of models that do not include the Keplerian hypothesis.

Chapter 4

Discussion

4.1 The thickness of sub-Keplerian discs

Before discussing the results reported in chapter 3, it is useful to describe some of the features of the disc models produced in this work. In Keplerian models the *aspect ratio* of the disc is usually represented by the ratio H/r of the disk thickness to disc radius r. In a standard disc model, the relation connecting the disc thickness H to the disc radius r is:

$$H/r = c_s/v_{kepl} \tag{4.1}$$

where c_s is the sound velocity and v_{kepl} is the Keplerian velocity at the disc outer edge. Such relation correlates the disc geometry to a tight Keplerian kinematic condition. In the Keplerian disc model developed here, the velocity of particles at the injectors positions is $v_{kepl} = 0.55$ in the units specified in section 2.1, $c_s = 0.05$ being the sound speed, thus we obtain:
$H/r \simeq 0.05/0.55 \ \sim 0.09$.

Generally this evaluation applies to a thin disc, where the hypothesis of vertical hydrostatic equilibrium is taken into account (Terquem et al., 2000). If this relation is translated also to sub-Keplerian modelling, it gives:
$H/r \simeq 0.12, 0.18, 0.36$ for $j = 54, 36, 18$ respectively.

Despite the rough indication that these results give on the disc geometry, these disc spreads are not strictly correct whenever turbulence and sub-Keplerian conditions are taken into account. The results of this work deal with protoplanet migration in a protoplanetary accretion disc around a pre-main sequence star, according to the hypothesis that the accretion process is not strictly Keplerian. The Keplerian constraint is often used in computational models of accretion protoplanetary accretion discs on the basis of observational features that can be reproduced with Keplerian discs. But it is sustainable if pressure and other forces are not able to significantly modify an initially Keplerian distribution of velocities. Once an exploration of models produces by releasing the Keplerian constraint is carried out, the comparison with "standard" can show significant differences.

4.2 Keplerian versus sub-Keplerian discs

Concerning the difference between the faster migration in sub-Keplerian models and slower migration in Keplerian ones, we can notice that: in sub-Keplerian models the most important contribution to downward migration seems to come from momentum transfer between the gas particles and the protoplanet; the sub-Keplerian specific angular momentum j_z of the injected SPH particles induces an average decrease of the planet's specific angular momentum l_z, until the protoplanet reaches the accretion disc centrifugal barrier; an initially Keplerian distribution of gas particles velocities, like in the Keplerian models described in this work, makes this effect less important, particularly with the Jovian planet. Models *kepl_a* and *kepl_b* show in fact a slow outward migration, despite the opening of a density gap. This result is different from classical views on the subject, which connect the opening of a density gap to a viscosity driven downward migration (type II migration), but without physical viscosity the result can be different.

Concerning the *type III* migration mechanism suggested by Papaloizou et al. (2007) and briefly introduced in section 1.1, it can be said that this effect might actually be present in the models presented here, but it is not the main migration mechanism, at least in sub-Keplerian models. The main migration "engine" of type III migration process is provided by material flowing through the co-orbital region, that cause some momentum transfer towards the protoplanet. Nevertheless, in sub-Keplerian models, the momentum transfer from the gas to the protoplanet due to gas particle capture can account for the migration rate observed in the results. To understand why, a rough estimate of the specific angular momentum change due to the capture of one disc SPH particle can be done as follows:

let l, j, M and m be the specific angular momentum and mass of the protoplanet and of the gas particle respectively; angular momentum conservation after particle capture leads to

$$\Delta l = \frac{m(j-l)}{M+m} \simeq \frac{m}{M}(j-l) \quad \text{for} \quad \frac{m}{M} << 1; \tag{4.2}$$

referring, as an example, to model 36*c*, the planet is at an initial radial distance of 100 in a circular Keplerian orbit, with $l_{initial} = 62.8$, $m/M = 10^{-4}$ and $j = 36$. Thus, after a single particle capture, eq. (4.2) gives $\Delta l \sim -2.7 \times 10^{-3}$.

Considering that about 10^5 particles are captured during the simulation with model 36*c* before the angular momentum is reduced to about one half of the initial value (not all of them will have preserved the $j = 36$ before capture), the momentum transfer due to particle capture is perfectly able to account for the observed rapid migration.

In Keplerian models (from *kepl_a* to *kepl_d*) particle captures can both induce an increase or decrease of the protoplanet angular momentum, and a flow of particles through the co-orbital region is visible (fig. 3.9), so type III mechanism might actually play a role. Notice however that the above specified flowing particles are moving towards smaller orbits, so they are mostly loosing angular momentum, giving it to the protoplanet. This might actually be the reason for the slowly increasing angular momentum of the protoplanet in $kepl\_a, b$ models. But, given that particle captures are present in all single-planet models, we cannot have pure type III migration anyway.

4.3 The effect of the pseudo-atmosphere

The results also lead our attention to the secondary role of the presence of a "pseudo-atmosphere" surrounding the protoplanet, with the aim to discover whether the cumulative interaction of the pseudo-atmosphere with the accretion disc could be also relevant.
The impact on the protoplanets is visible in some of the models including this effect, particularly those with the a less massive protoplanet (look at the difference between models $54c$ and $54d$, shown in fig. 3.6), but it never appears crucial in determining the main results.
The slightly faster migration rate shown by models without the pseudo-atmosphere is actually expected, because the pseudo-atmosphere adds a repulsive pressure interaction between the protoplanet and the gas. This hinders the gas particle captures by the protoplanet. Since the main part of the migration effect in all the models is due to momentum transfer between the infalling particles and the protoplanets when the former are captured, a lower capture rate brings a lower migration rate.

4.4 Migration braking by shock waves

Particularly interesting is the result reported by the c, d models, where the radial migration breaks down close to $\sim$ 15; 20; 45 stellar radii, for $j = 18; 36; 54$ respectively. This effect is probably due to the interaction of the protoplanet with the outward propagating waves coming from inner zones (fig. 3.14-3.15), where the centrifugal barrier is located in the sub-Keplerian models. These results show that, despite the sub-Keplerian

and more realistic conditions, planetary migration could be slowed and even halted. Once the protoplanet migration is halted for a sufficient amount of time, subsequent disc extinction could freeze the protoplanet orbital parameters. Of course, due to a much higher inertia, Jovian planets evolve much more slowly.
A correct analysis of the times and mechanisms involved in such a picture requires a detailed quantitative study of momentum transfer due to shock waves, and it provides a topic for a future work on the subject.

4.5 Comparison with previous results

For a comparison with other results we can refer to the study performed by Schäfer et al. (2004), since they used SPH to simulate accretion disc hydrodynamics, even if some differences have to be remarked:

- they use a different numerical method to avoid particle mutual penetration, relying on XSPH with a bulk viscosity contribution to the viscous stress tensor;

- they simulate physical viscous discs according to Shakura and Sunyaev (1973) prescription whilst this work describes inviscid discs;

- they use an isothermal equation of state while a classical ideal gas equation with variable thermal energy per unit mass is used here;

- their initial velocity distribution is Keplerian.

Their estimates give a decrease of the planet distance to the star of about 1 AU (from 5.2 AU to 4.1 AU) in about 30000 years for a Jovian planet. This leads to a rate of
$Da/Dt \sim 3.3 \times 10^{-5}$ AU y^{-1}.
They also conclude that migration is braked by disc mass loss, which means a lowering of the disc density and of the gravitational interaction.

An estimate with physical units can here be obtained by inserting in the dimensionless model the following reference physical units: central star mass $M_0 = 1M_\odot$; stellar radius from typical T-Tauri stars (Bertout, 1989) $R_0 \sim 2R_\odot$; the basic unit for time is $T_0 \sim 2.8 \times 10^4$ s. With the above specified choices the sub-Keplerian models with $j = 18; 36; 54$ give migration rates of $Da/Dt \sim 8 \times 10^{-5}; 5.3\times^{-5}; 3.4 \times 10^{-5}$ AU y^{-1} respectively.
We notice that for $j = 54$ (the less sub-Keplerian model) the migration rate is similar to the average migration rate obtained by Schäfer et al. (2004), even if here the starting distance is about 1 AU, with the above specified choices for physical units. More important, here the braking effect is due to a completely different mechanism based on turbulence, outward propagation of bouncing waves and changing of the average momentum transferred to the planet during gas particle captures, and a significant lowering of the disc density is not observed in the time interval of both Keplerian and sub-Keplerian models.

4.6 Eccentricity

Even if it is not the main topic of this paper, let's draw some comments on the behaviour of eccentricity shown in the bottom rectangles of fig. 3.1-3.8. For Jupiter-like planets the orbits remain almost circular, with values around 10^{-5}, while for Earth-like planets some eccentricity enhancing effect is visible in sub-Keplerian models, but the behaviour is quite complex and a more stable value is obtained in late migration phases, with values in the $0.01 - 0.02$ range. Similar behaviours are observed in two-planets models.

4.7 Preliminary comments on two-planets results

The study on multi-planetary models with accretion disc is still under development, and current results are considered preliminary, but some considerations can be outlined here on the results described in the previous chapter. If we look at the orbital evolution of each planet in the two-planets models, there are some similarities with what observed in single planet models. This is mostly true for Earth-like protoplanets for which the planet-planet interaction is less important. The main mechanism for planet migration is still based on particle captures by the protoplanets and the resulting specific angular momentum variation due to momentum conservation, but the observed migration times are different. This could be due to the mutual planet-planet interaction, the external protoplanet can in fact perturb the disc gas flux, producing effects on the inner protoplanet.

Concerning the "beats" features observed in models a, they are not linked to the presence of the disc. To confirm their nature due to planet-planet interaction we ran a simplified simulation including the two-planets with the same initial conditions, but without the accretion disc. The orbital parameters of the two planets were tracked and compared with the results of the main simulations. In fig. 4.1 the orbital parameters evolution of the external protoplanets obtained with the accretion disc (model 2_36a) and without it, are compared. The semi-major axes and the specific angular momenta start to show sensible differences after 12-13 orbits, while the graphs are partially overlapped at earlier times. It is after this time period that the transport effects of the accretion disc on the planets orbits start to become evident. All the "beats" features are instead present in the simulation without the disc.

The peculiar behaviour of model 3.20, where a sudden change of orbital parameters is observed, is probably a case of *slingshot effect*, where the internal Jovian planet can completely alter the orbit of the external Terrestrial protoplanet. This confirm the hypothesis that massive planets close the central star (distance less that 1 AU) could be able to "clean" all less massive planets in more external orbits, if enough time passes. The simulations

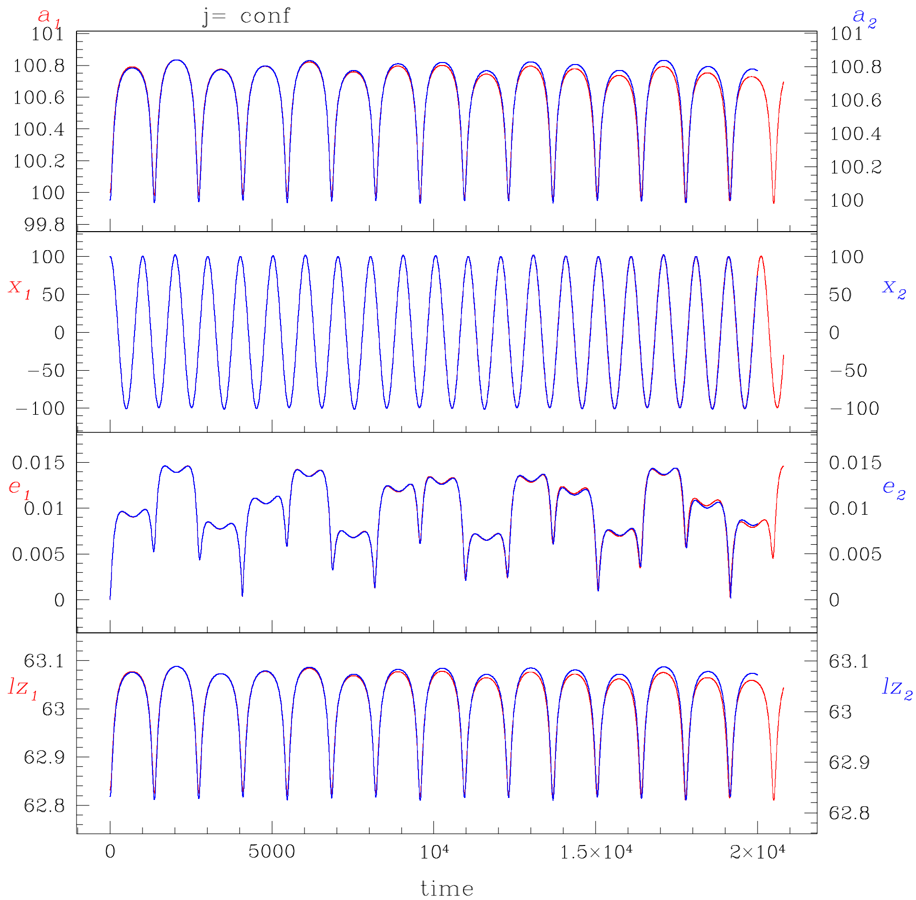

Figure 4.1: Orbital parameters evolution: comparison between the simplified model with two Jovian planets and no accretion disc and the "full" hydrodynamical model 2_36a including the accretion disc. Notice the partial overlap of graphs (see text).

should be run for a much longer period to confirm such a result. Deeper analysis of two-planets models is left for a future work.

In the next appendix chapter, a numerical test on the dissipative effects of artificial viscosity present in SPH code used here, is described. Even if not directly linked to the accretion disc evolution details, the test gives an interesting view on some important numerical and physical features of the code used for this work, and of other inviscid codes based on SPH.

Chapter 5

On the dissipative effect of artificial viscosity

5.1 The kinematic viscosity coefficient of artificial viscosity

The models described in this thesis are technically considered as physically inviscid, since they are based on the Euler equations. Artificial viscosity (Monaghan, 1992) is necessarily introduced in the models to resolve shocks numerically, to avoid spurious heating and to handle fluid discontinuities. These numerical issues usually happens during gas compression, so the artificial viscosity is set to have effect when gas particles approach each other, while it is set to zero when they move away from each other. Artificial viscosity vanishes also when the limit value of the particle interpolation domain goes to zero.

Despite the name, the aim of artificial viscosity is not to include dissipative effects into the model, but dissipation is present as a side effect. Meglicki et al. (1993); Drimmel (1996); Murray (1996); Okazaki et al. (2002) demonstrated that the linear component of the artificial viscosity, in the continuum limit, yields a viscous shear force. Murray (1996) and Okazaki et al.

(2002) explicitly formulated such an artificial viscosity contribution in momentum and energy equations, finding an analogy between the shear viscosity generated by the linear artificial viscosity term and the well-known Shakura and Sunyaev (1973) shear viscosity in the continuum limit. In the SPH method, the quadratic (β_{SPH}, von Neumann-Rychtmyer like viscosity) artificial viscosity term is used in order to handle structures. An analytical formulation, describing the numerical artificial viscosity coefficient, is reported in Molteni et al. (1991):

$$\nu_{num} = c_s h \tag{5.1}$$

where c_s is the sound velocity, and h is the SPH smoothing length. Therefore, in the modelling used in this work, there is a radial transport process due to the role of the artificial viscosity.
Instead, Murray (1996) as well as Okazaki et al. (2002), gave an analytical formulation where $\nu < c_s h$ and in particular

$$\nu = \frac{1}{8}\alpha c_s h \tag{5.2}$$

and

$$\nu = 0.1 \alpha c_s h \tag{5.3}$$

respectively for shear flow component, where α is the same linear coefficient present in eq. (2.8). In both papers, the viscous force per unit mass in the continuum limit is given by:

$$\mathbf{F}_V = \frac{\alpha h \kappa}{2\rho}\left(\nabla \cdot (c_s \rho \mathbf{S}) + \nabla(c_s \rho \nabla \cdot \mathbf{v})\right) \tag{5.4}$$

where

$$S_{ij} = \frac{\partial v^i}{\partial x^j} + \frac{\partial v^j}{\partial x^i}$$

is the deformation tensor (Meglicki et al., 1993) and κ is a numerical factor, depending on the interpolation kernel. If density ρ and sound speed c_s are "constant" (their gradients with respect to the spatial coordinates are much smaller than the gradient of velocity)

$$\mathbf{F}_V = \frac{\kappa}{2}\alpha c_s h \left[\nabla^2\mathbf{v} + 2\nabla(\nabla\cdot\mathbf{v})\right] \tag{5.5}$$

Both Murray (1996) and Okazaki et al. (2002), under the hypothesis
$\nabla\cdot\mathbf{v} = 0$,
use a simplified version of eq. (5.5):

$$\mathbf{F}_V = \frac{\kappa}{2}\alpha c_s h \nabla^2\mathbf{v} \tag{5.6}$$

this expression allows to approximately describe the effects of shear dissipations due to "inviscid" SPH codes as a physical viscosity with a kinematic coefficient given by:

$$\nu = \frac{\kappa}{2}\alpha c_s h \tag{5.7}$$

For a viscous accretion disc described in the Shakura and Sunyaev (1973) prescription, the expression of kinematic viscosity is similar:

$$\nu_{SS} = \alpha_{SS} c_s H \tag{5.8}$$

Expressions (5.7) and (5.8) equal each other if

$$\alpha_{SS} = \frac{\kappa}{2}\alpha\frac{h}{H} \tag{5.9}$$

Murray (1996) and Okazaki et al. (2002) give different values for κ: 1/5 and 1/4 respectively, leading to eq. (5.2) and (5.3).

If we follow the arguments by Lanzafame (2008), an approximate quantitative estimate of the dissipative effect in the model used in this work can be obtained by using the values of H/r evaluated in section 4.1. We have the following:

$$\nu = \alpha_{SS} c_s H = c_s h \quad \rightarrow \quad \alpha_{SS} = h/H \tag{5.10}$$

Using the values of H/r estimated in section 4.1:
$\alpha_{SS} \simeq 2.5\times10^{-2}$; 1.9×10^{-2}; 1.3×10^{-2}; 6.4×10^{-3}
for Keplerian and $j = 54, 36, 18$ respectively.

Summarising, we have that the artificial viscosity produces shear viscosity effects with a kinematic coefficient given by:

$$\nu = kc_s h \tag{5.11}$$

where the proportionality constant k is suggested to be 1 by Molteni et al. (1991), 1/8 (with $\alpha = 1$) by Murray (1996) and 1/10 by Okazaki et al. (2002). While Murray (1996) compared numerical to analytical results in the case of the *spreading ring test*, Okazaki et al. (2002) limited their conclusion only to mathematical aspects. The approximate estimates obtained above with eq. (5.10) are based on the choice $k = 1$.

5.2 The spreading ring test

The results of a numerical *spreading ring test* are reported here. This test is used to estimate the value of the parameter k defined in section 5.1, and to allow a comparison between the effects produced by the implementation of artificial viscosity used in this thesis and the effects produced by physical shear viscosity. The test compares a simulated spreading ring of gas particles (Speith and Riffert, 1999; Speith and Kley, 2003) with its approximate analytical solution.

The analytical solution is described by Flebbe et al. (1994); Pringle (1981) and it is based on the modified Bessel function of order 1/4. The hypotheses under which the analytical solution is valid are the followings (Pringle, 1981; Speith and Riffert, 1999):

- a mass of gas, with two dimensional geometry (or three dimensional with cylindrical symmetry) moves inside a central potential well;
- "thin" disc-like evolving structure of the gas, with initial ring-shaped distribution;
- thermal time-scale much shorter than viscous time-scale, meaning that

angular momentum transport is "slow" and the disc is almost isothermal;

- dynamical time-scale much shorter than viscous time-scale, this implies that the time for gas particle inflow towards the force centre, due to viscous angular momentum transport, is much longer than gas particle orbital periods;

- constant kinematic viscosity ν;

- the gas has no pressure, all transport effects are due to viscosity.

Under these hypotheses, the time dependence of the surface mass density Σ is given by:

$$\Sigma(x,\tau) = \frac{M}{\pi R_0^2} \frac{1}{\tau x^{-1/4}} I_{1/4}\left(\frac{2x}{\tau}\right) exp\left(-\frac{1+x^2}{\tau}\right) \tag{5.12}$$

where:

$$\Sigma(x,\tau=0) = M\frac{\delta(r-R_0)}{2\pi R_0} \tag{5.13}$$

is the initial δ distribution at time $\tau = 0$, r is the radial coordinate, M is the total mass of the gas, R_0 is the radius of the initial ring, $x = r/R_0$ is the dimensionless radial coordinate, $I_{1/4}$ is the *Modified Bessel function* of order 1/4, while:

$$\tau = 12\nu t R_0^{-2} \tag{5.14}$$

is the time in units of the viscous time-scale.

The above listed hypotheses are artificial in a realistic situation. Therefore, the analytical solution cannot be expected to exactly match the results of a simulation if the physical conditions of the numerical model significantly deviate from the above listed hypotheses. Nevertheless, a numerical test can both help to analyse the dissipative effect of artificial viscosity and to find an estimate of the parameter k. This estimate is found by trying various numerical simulations with different k values, and by checking which of these values fit the known analytical solution described above. A *chi square* test is used to examine the fits.

5.2.1 Testing model

The code used for the test is the same SPH code used for the simulation of accretion discs, with some adjustments. The initial configuration is a Keplerian annulus ring, composed of 40000 Keplerian SPH particles as in Speith and Kley (2003), and the *smoothing length* is $h = 0.09$ as in Speith and Riffert (1999). The initial particle spatial distribution is produced by randomly generating the polar coordinates of the particles, with proper probability distributions. A flat probability distribution is used for the coordinate ϕ, while the probability profile for the radial coordinate is set according to eq. (5.12), with $\tau_0 = 0.017$. A zero initial value for the dimensionless time τ cannot be used, since eq. (5.12) gives a δ-Dirac function for $\tau = 0$.

The k proportionality constant between ν and $c_s h$ becomes a proportionality constant between the simulation time t and the dimensionless time τ (eq. 5.14). Simulations have been performed with k values in the range $0.1 - 1$ (the analysed values are: 0.1, 0.2, 0.3, 0.35, 0.4, 0.45, 0.5, 0.55, 0.6, 0.65, 0.7, 0.8, 1.0). The larger k, the shorter t to get the same τ.

Each simulation has been carried out for a τ interval $(0.017 - 0.2)$ that is similar to what reported in Speith and Kley (2003). Going further in time would, in many cases, bring to particle distributions with many isolated particles. Nevertheless, there are some differences among the simulations performed by Murray (1996); Speith and Riffert (1999); Speith and Kley (2003) and those presented here:

- this test is concerned with the shear dissipative effects of artificial viscosity in “inviscid” SPH approach. Other works refer to the instabilities produced by physical viscosity, using a tensor based formalism for the viscosity;

- the spreading ring tests are usually done in pressure-less conditions, but, in this work, while gas pressure is not directly applied to gas particles as a driving force, the model is not totally pressure-less, since artificial viscosity is treated as a pressure term in the momentum equation. Moreover gas pressure is used to calculate the sound speed c_s. Even temperature is not constant, in order to correctly and more realistically evaluate c_s in the ring structure (Costa et al., 2010);

- the sound speed c_s is not constant, but the $\tau - t$ conversion is done on the basis of the initial value of $c_s = 0.05$ in dimensionless units.

Throughout the SPH modelling $\alpha = \beta = 1$ ($R_0 = 1$).

5.2.2 Test results

Two-dimensional representations of the ring evolution for $k = 0.2, 0.5, 0.8$ are given in fig. 5.1, in columns a, b and c respectively, where the gas particle positions are shown for four increasing τ values (0.017, 0.056, 0.162, 0.198). It is evident that the "speed" (in terms of the dimensionless time τ) of the ring dissipation and radial transport processes decreases with increasing k. Figures 5.2-5.4 show the comparison of analytical mass-density radial distributions to its SPH numerical counterparts at various τ values, and for $k = 0.2, 0.5, 0.8$ respectively. While the analytically obtained densities are easily expressed as a function of r through the distribution function (5.12), azimuthal averages are used for distributions coming from SPH simulations, since the numerical results are given as xy point distributions of particles of equal mass.

In order to find the best approximation for the coefficient k, a χ^2 test has been applied to the numerically obtained particle distributions, testing their fit to the theoretical analytical distribution. Tests have been performed by

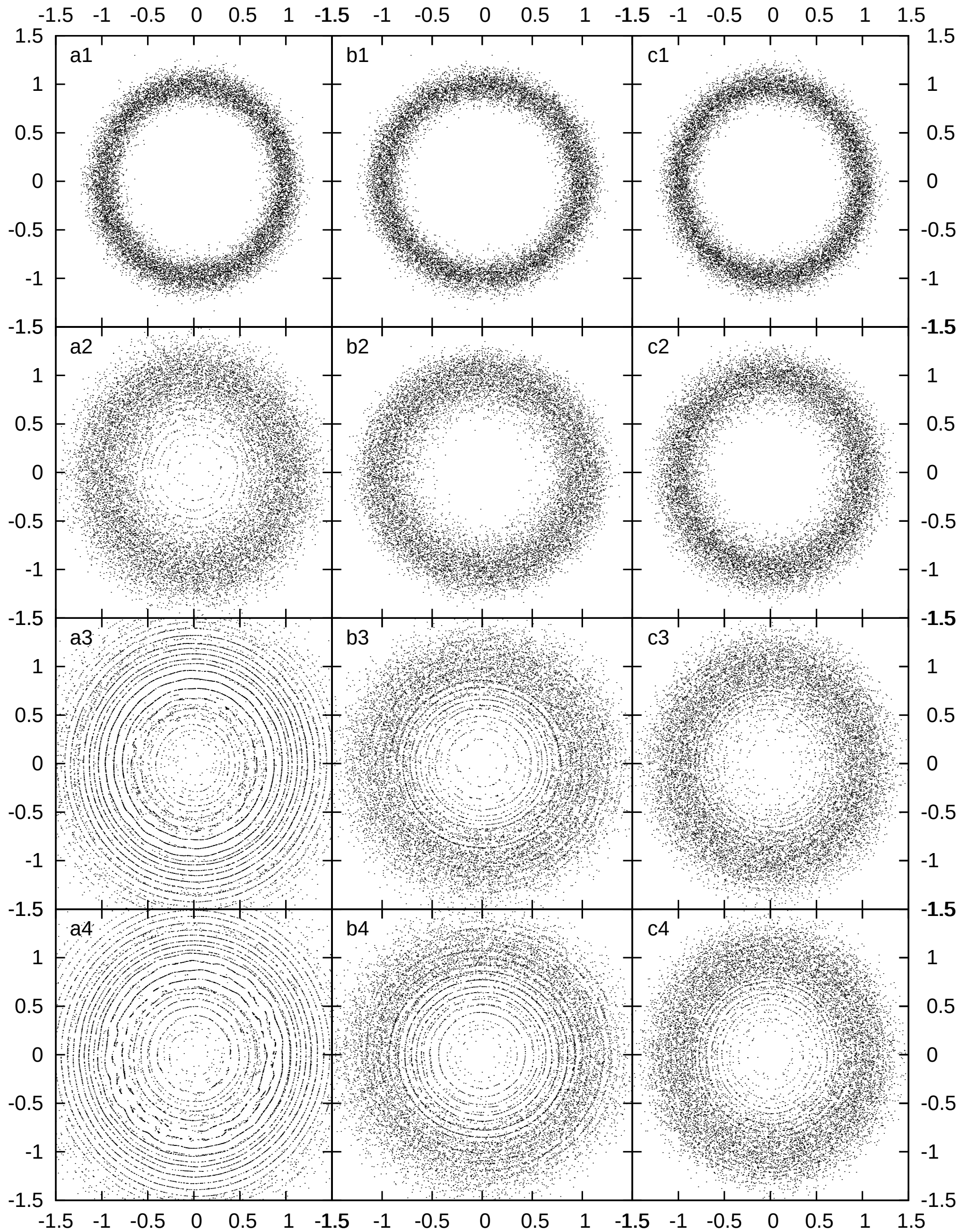

Figure 5.1: xy-ring structures for $k = 0.2$ (a), $k = 0.5$ (b) and $k = 0.8$ (c) at $\tau = 0.017, 0.056, 0.162, 0.198$ (squares numbered 1, 2, 3 and 4 respectively).

dividing the radial distance of the particles in intervals. The intervals are chosen in order to have ~ 100 particles in each interval according to the theoretical distribution.

The graphs reported in figures 5.1-5.4 involve a selection of k values. The complete set of data has been used to build fig. 5.5, where the *reduced* χ^2 (χ^2_r) values as a function of k are plotted. The data corresponding to the same τ value are identified with a common label, and they are connected trough a smooth curve obtained trough 3rd order polynomial best-fits.

The curve connecting the points corresponding to the initial $\tau_0 = 0.017$, is

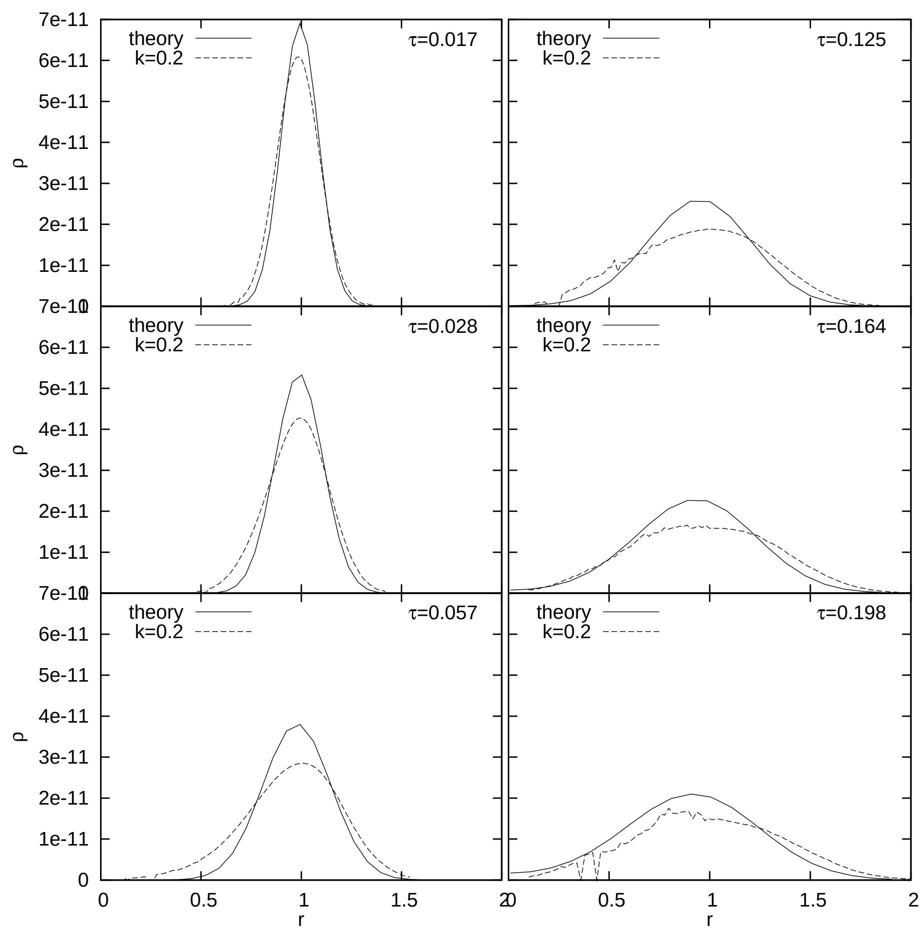

Figure 5.2: Azimuthally averaged density profiles, as a function of radial distance r, for $k = 0.2$, compared to the analytical solutions, at various τ (0.017 to 0.198).

expected to be a straight horizontal line, but some small oscillations in the χ^2_r values are observed. This effect is unavoidable, since each distribution is created with a random generation procedure following the theoretical probability profile given by eq. (5.12). A test performed by randomly generating

10 times the initial distribution at $\tau_0 = 0.017$ gave variable initial χ_r^2 values, with a standard deviation in the order of 5%.

The analysis of fig. 5.5 shows that the deviations among analytical and

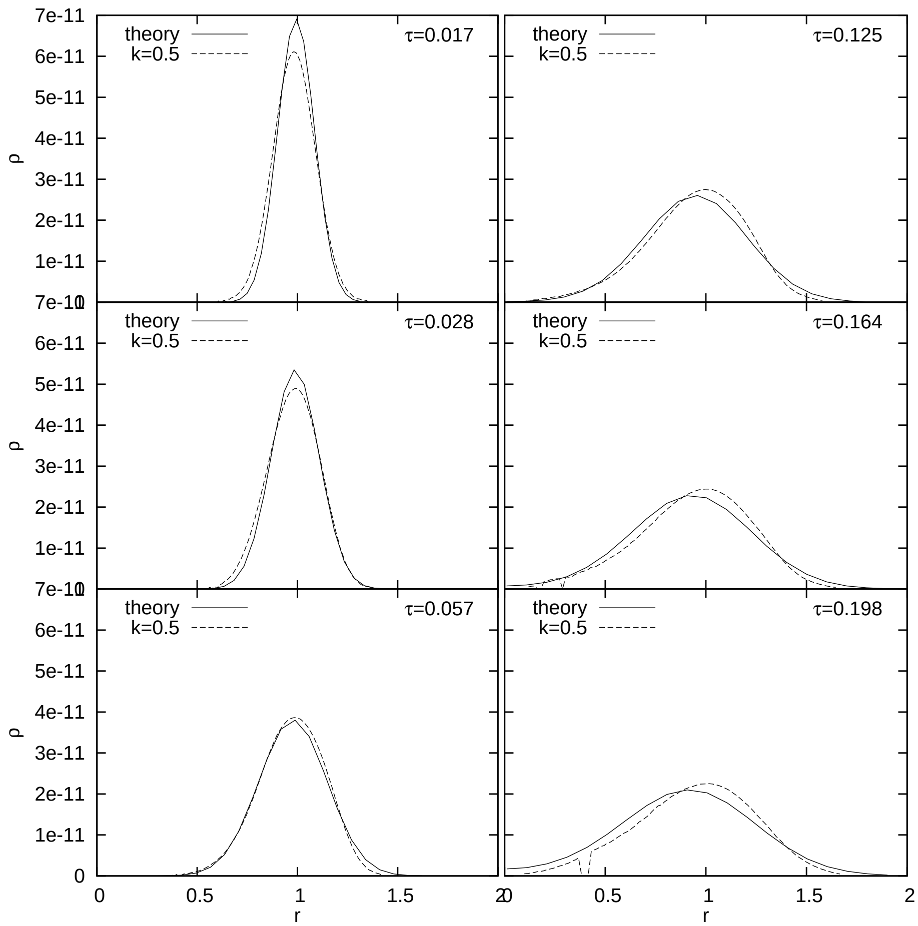

Figure 5.3: Azimuthally averaged density profiles, as a function of radial distance r, for $k = 0.5$, compared to the analytical solutions, at various τ values (0.017 to 0.198).

numerical distributions progresse with τ as expected. The approximation producing the analytical solution becomes in fact less and less acceptable with increasing τ. The increase of such discrepancies is monotonic but not quite linear with τ.

In the above results it is evident that:

1. The spreading of the initial ring structure is "faster", measuring the speed according to the dimensionless time τ, when higher k values are

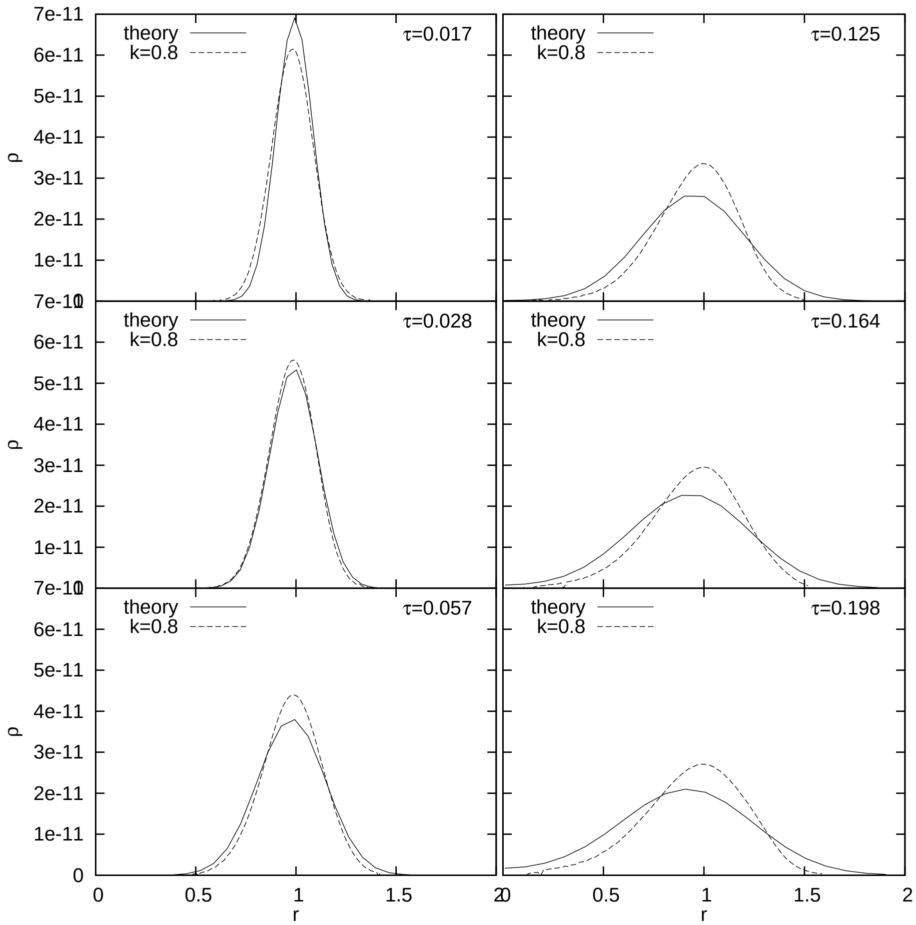

Figure 5.4: Azimuthally averaged density profiles, as a function of radial distance r, for $k = 0.8$, compared to the analytical solutions, at various τ values (0.017 to 0.198).

chosen;

2. the value of χ_r^2 generally increases with increasing τ;

3. for each τ there is a minimum in χ_r^2, and this minimum is typically located in the $0.4 - 0.6$ range;

4. for the highest value of τ the situation becomes less clear and k_{min} is closer to 1.

Point 1 is expected, because k is directly related to the $\tau - t$ conversion as explained above. Point 2 is interpreted by remembering that the basic

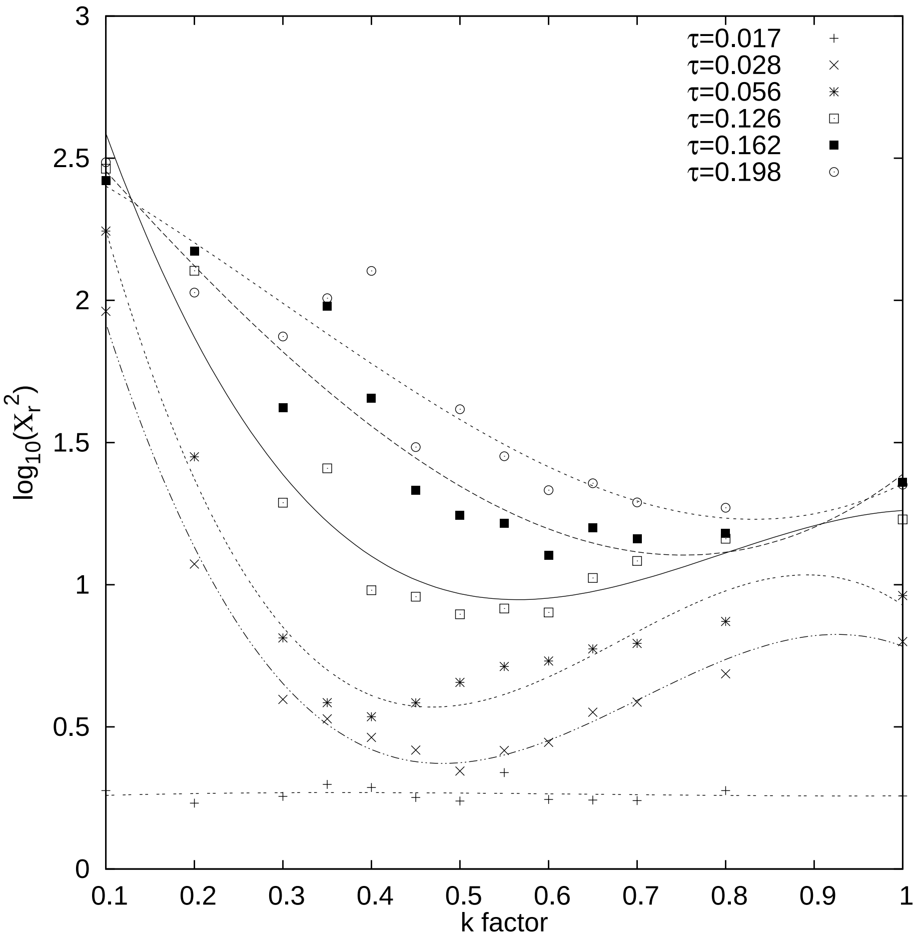

Figure 5.5: Reduced χ^2 values calculated on the gas SPH particle distribution over the radial distance r, when compared to the theoretical distribution given by eq. (5.12). χ_r^2 is plotted as a function of k (see text), for each tabulated τ value.

hypotheses for the theoretical analytical solution, are not strictly satisfied, therefore the numerical solution can diverge from the theoretical one over time. As far as point 3 is concerned, the presence of a minimum in the χ_r^2 distribution gives an indication of a "best fit" value for k.

The rough indication coming out from fig. 5.5 is $k_{best-fit} \sim 0.4 - 0.6$, and it also appears that a constant k, good in all situations, maybe does not really exist. A confirmation to this is in point 4.

The search for a "constant" of proportionality like k, is the consequence of the above described comparison between the artificial viscosity in "inviscid"

SPH implementation and physical viscosity, but the two effects work differently, and a simple scheme where $\nu \propto c_s h$ is not always reliable in describing the behaviour of artificial viscosity, being this interpretation based also on the somewhat simplistic $\nabla \cdot \mathbf{v} = 0$ hypothesis.

The results obtained for k is higher than both the indications by Murray (1996); Okazaki et al. (2002). The reasons for this are probably the followings:

- they conducted their spreading ring tests for very small values of τ compared to what is done here, so they did not explore the worsening of the fit between analytical and numerical results with increasing τ;

- at "low" τ values, in the order of 10^{-4}, the particles in the gas ring are very close to each other. In this situation the typical cubic polynomial kernel used in SPH underestimates pressure gradients, it's a known issue which in confirmed in Lanzafame (2010). At later times the average distance between SPH particles increases and higher pressure gradients can arise, making the dissipative effects of artificial viscosity stronger, thus enhancing the constant of proportionality k.

A confirmation of the above listed observations is present in fig. 5.6, where the results of a similar test is reported. In this case the initial value of τ is much smaller, $\tau_0 = 1.6 \cdot 10^{-4}$, and smaller values of τ are analysed. The figure is organised in the same way as fig. 5.5. This time the "bet-fit" value of k is in the $0.1 - 0.2$ range, in line with what suggested by Murray (1996); Okazaki et al. (2002).

5.2.3 The role of artificial viscosity parameters

The choice $\alpha = 1$, $\beta = 1$, as in Molteni et al. (1991) is intended to correctly treat gas shocks in a turbulent environment. In a spreading ring test, a

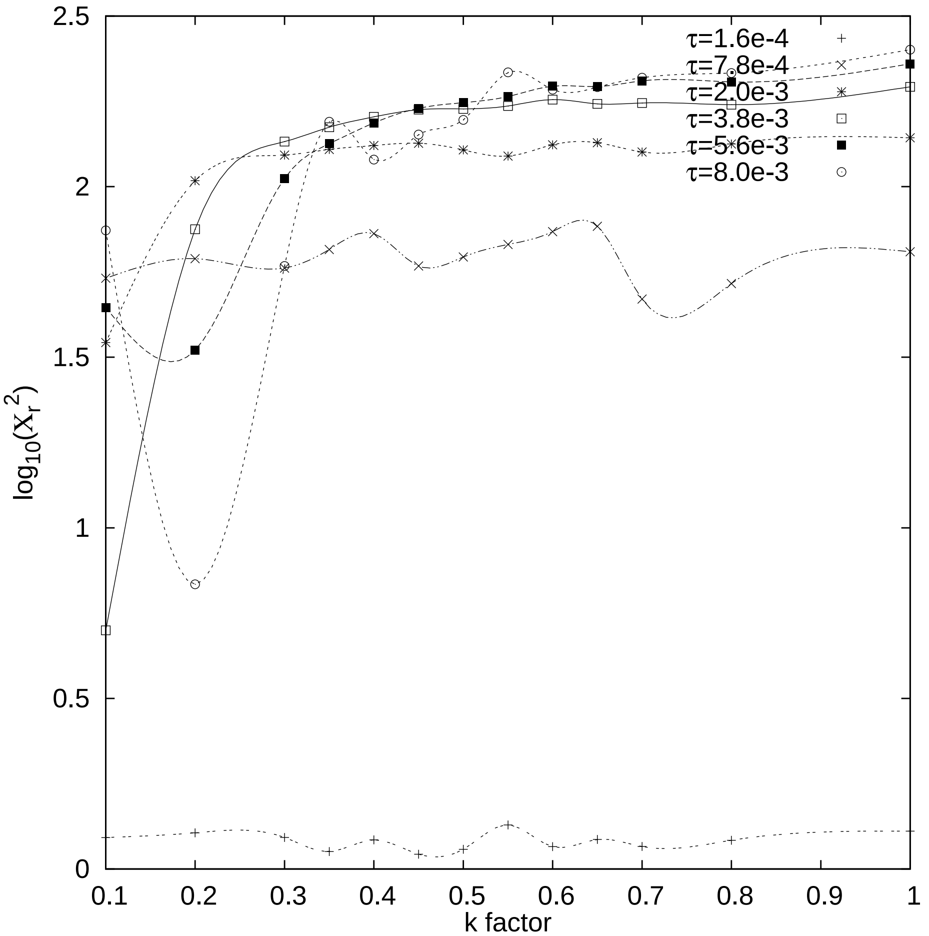

Figure 5.6: Reduced χ^2 values calculated on the gas SPH particle distribution over the radial distance r, when compared to the theoretical distribution given by eq. (5.12). χ^2_r is plotted as a function of k, for each tabulated τ value. This results are obtained taking $\tau_0 = 1.6 \cdot 10^{-4}$ as a starting value. Compared to fig. 5.5, the minimum of χ^2_r is here obtained for $k \sim 0.1 - 0.2$.

lower α value and a suppression of the quadratic term ($\beta = 0$) is suggested in some cases as a more acceptable choice.

In order to test the effects of different choices for α, two additional simulations were done, the first with $\alpha = 0.5$ and the second $\alpha = 2.0$, but the relation $\nu = kc_sh$ given in eq. (5.11) has been changed in:

$$\nu = k\alpha c_s h \tag{5.15}$$

This variation allows to change α without changing the value of the proportionality constant $k\alpha$. The two simulations have been performed with $\alpha = 0.5 \quad k = 1.0$ and $\alpha = 2.0 \quad k = 0.25$ respectively, thus the total proportionality constant has been maintained equal to $k\alpha = 0.5$, according to the minimum present in fig. 5.5. This test is interesting because, while the total proportionality constant mainly affects the $\tau - t$ conversion, a change in α may actually change the behaviour of viscosity.

τ	$^{(a)}$ $k = 1.0$ $\alpha = 0.5$	$^{(b)}$ $k = 0.5$ $\alpha = 1$	$^{(c)}$ $k = 0.25$ $\alpha = 2.0$
0.017	1.74	1.73	1.73
0.028	2.29	2.21	2.31
0.056	5.13	4.53	3.64
0.126	9.27	7.87	6.53
0.162	18.5	17.5	18.1
0.198	43.1	41.4	47.2

Table 5.1: χ_r^2 values obtained with the three models: (a) $k = 1.0$ $\alpha = 0.5$; (b) $k = 0.5$ $\alpha = 1$; (c) $k = 0.25$ $\alpha = 2.0$

Results in the form of averaged density profiles are shown in figures 5.7-5.8. They appear very similar to the results shown in fig. 5.3. A comparison of the χ_r^2 values obtained with these two simulations and the previous one with $k = 0.5$ is summarised in table 5.1. There are some differences, with slightly better results for $\alpha = 2$ when $\tau \lesssim 0.13$ and for $\alpha = 0.5$ when $\tau \gtrsim 0.13$. Nevertheless, the differences are quite small compared to the general variations observed by changing τ.

These last results show that there is some arbitrariness in interpreting the effects of the various choices for the proportionality constant $k\alpha$ in eq. (5.15). It appears that the relation $\tau \sim 0.5 c_s h$ gives the best results concerning the correct representation of dissipative and radial transport effects of artificial

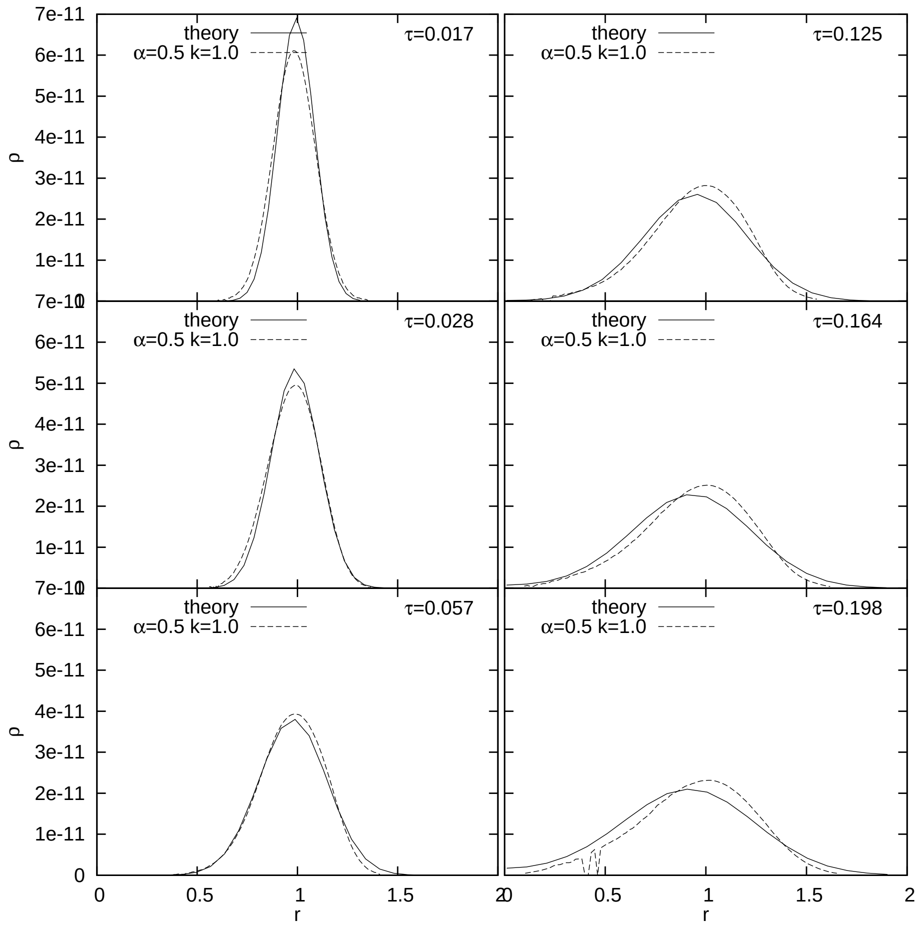

Figure 5.7: Azimuthally averaged density profiles, as a function of radial distance r, for $\alpha = 0.5$, $k = 1.0$, compared to the analytical solutions, at various τ values (0.017 to 0.198).

viscosity. However the 0.5 factor could be interpreted either with a proper choice of k or α. In the last case, a lower α value with respect to the "standard" $\alpha = 1$ can be chosen, when correct shock treatment is not a concern.

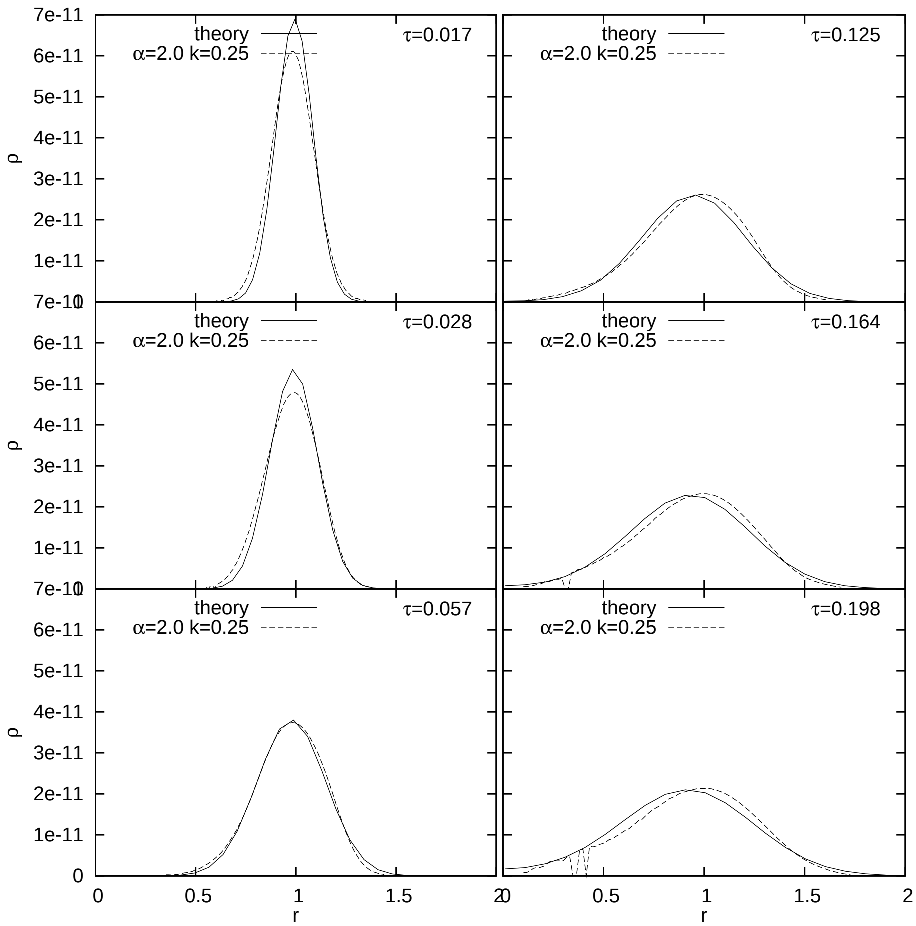

Figure 5.8: Azimuthally averaged density profiles, as a function of radial distance r, for $\alpha = 2.0$, $k = 0.25$, compared to the analytical solutions, at various τ values (0.017 to 0.198).

5.3 Acknowledgements

Un ringraziamento particolare va a Giuseppe Lanzafame per la sua infinita pazienza ed i preziosi consigli nel seguirmi durante lo svolgimento di questo lavoro di tesi. Ringrazio anche Alessandro Grillo per l'indispensabile supporto nell'uso dell'infrastruttura GRID di COMETA, mediante la quale sono state eseguite le simulazioni numeriche.

Bibliography

Artymowicz, P., Dec. 2004. Dynamics of Gaseous Disks with Planets. In: L. Caroff, L. J. Moon, D. Backman, & E. Praton (Ed.), Debris Disks and the Formation of Planets. Vol. 324 of Astronomical Society of the Pacific Conference Series. pp. 39–+.

Bertout, C., 1989. T Tauri stars - Wild as dust. ARA&A27, 351–395.

Chakrabarti, S. K., Molteni, D., Nov. 1993. Smoothed Particle Hydrodynamics Confronts Theory: Formation of Standing Shocks in Accretion Disks and Winds around Black Holes. ApJ 417, 671–+.

Costa, V., Pirronello, V., Belvedere, G., Del Popolo, A., Molteni, D., Lanzafame, G., Feb. 2010. How initial and boundary conditions affect protoplanetary migration in a turbulent sub-Keplerian accretion disc: 2D non-viscous SPH simulations. MNRAS 401, 2388–2398.

Cresswell, P., Nelson, R. P., May 2006. On the evolution of multiple protoplanets embedded in a protostellar disc. A&A 450, 833–853.

Cresswell, P., Nelson, R. P., May 2008. Three-dimensional simulations of multiple protoplanets embedded in a protostellar disc. A&A 482, 677–690.

Crida, A., Kley, W., Sandor, Z., Jul. 2007. Damping eccentricity of resonant exoplanets. In: J. Bouvier, A. Chalabaev, & C. Charbonnel (Ed.), SF2A-2007: Proceedings of the Annual meeting of the French Society of Astronomy and Astrophysics. pp. 398–+.

Crida, A., Sándor, Z., Kley, W., May 2008. Influence of an inner disc on the orbital evolution of massive planets migrating in resonance. A&A 483, 325–337.

D'Angelo, G., Henning, T., Kley, W., Apr. 2002. Nested-grid calculations of disk-planet interaction. A&A 385, 647–670.

D'Angelo, G., Kley, W., Henning, T., Mar. 2003. Orbital Migration and Mass Accretion of Protoplanets in Three-dimensional Global Computations with Nested Grids. ApJ 586, 540–561.

D'Angelo, G., Lubow, S. H., Bate, M. R., Dec. 2006. Evolution of Giant Planets in Eccentric Disks. ApJ 652, 1698–1714.

de Val-Borro, M., Edgar, R. G., Artymowicz, P., Ciecielag, P., Cresswell, P., D'Angelo, G., Delgado-Donate, E. J., Dirksen, G., Fromang, S., Gawryszczak, A., Klahr, H., Kley, W., Lyra, W., Masset, F., Mellema, G., Nelson, R. P., Paardekooper, S., Peplinski, A., Pierens, A., Plewa, T., Rice, K., Schäfer, C., Speith, R., Aug. 2006. A comparative study of disc-planet interaction. MNRAS 370, 529–558.

Drimmel, R., Oct. 1996. Viscous damping in self-gravitating accretion discs. MNRAS 282, 982–1004.

Flebbe, O., Muenzel, S., Herold, H., Riffert, H., Ruder, H., Aug. 1994. Smoothed Particle Hydrodynamics: Physical viscosity and the simulation of accretion disks. ApJ 431, 754–760.

Goldreich, P., Tremaine, S., Nov. 1979. The excitation of density waves at the Lindblad and corotation resonances by an external potential. ApJ 233, 857–871.

Goldreich, P., Tremaine, S., Oct. 1980. Disk-satellite interactions. ApJ 241, 425–441.

Gullbring, E., Hartmann, L., Briceno, C., Calvet, N., Jan. 1998. Disk Accretion Rates for T Tauri Stars. ApJ 492, 323–+.

Hartigan, P., Edwards, S., Ghandour, L., Oct. 1995. Disk Accretion and Mass Loss from Young Stars. ApJ 452, 736–+.

Hartmann, L., 2000. Accretion Disks (Invited Review). In: G. Garzón, C. Eiroa, D. de Winter, & T. J. Mahoney (Ed.), Disks, Planetesimals, and Planets. Vol. 219 of Astronomical Society of the Pacific Conference Series. pp. 95–+.

Jiang, I., Yeh, L., Feb. 2007. A Possible Correlation between the Gaseous Drag Strength and Resonant Planetesimals in Planetary Systems. ApJ 656, 534–544.

Kley, W., 2000. The Orbital Evolution of Planets in Disks. In: G. Garzón, C. Eiroa, D. de Winter, & T. J. Mahoney (Ed.), Disks, Planetesimals, and Planets. Vol. 219 of Astronomical Society of the Pacific Conference Series. pp. 69–+.

Kley, W., Lee, M. H., Murray, N., Peale, S. J., Jul. 2005. Modeling the resonant planetary system GJ 876. A&A 437, 727–742.

Kley, W., Peitz, J., Bryden, G., Feb. 2004. Evolution of planetary systems in resonance. A&A 414, 735–747.

Kominami, J., Tanaka, H., Ida, S., Nov. 2005. Orbital evolution and accretion of protoplanets tidally interacting with a gas disk. I. Effects of interaction with planetesimals and other protoplanets. Icarus178, 540–552.

Lanzafame, G., Apr. 2008. Role of Compressibility, Turbulent Viscosity, and Mass-Transfer-Rate on Accretion Discs in Close Binaries. PASJ 60, 259–.

Lanzafame, G., Nov. 2010. An approach to solving the boundary free edge difficulties in SPH modelling: application to a viscous accretion disc in close binaries. MNRAS 408, 1551–1567.

Lanzafame, G., Cassaro, P., Schilliró, F., Costa, V., Belvedere, G., Zappalá, R. A., May 2008. The role of viscosity in AGN outflows in relation to jet periodicities. A&A 482, 473–482.

Lanzafame, G., Molteni, D., Chakrabarti, S. K., Sep. 1998. Smoothed particle hydrodynamic simulations of viscous accretion discs around black holes. MNRAS 299, 799–804.

Lecoanet, D., Adams, F. C., Bloch, A. M., Feb. 2009. Mean Motion Resonances in Extrasolar Planetary Systems With Turbulence, Interactions, and Damping. ApJ 692, 659–676.

Lin, D. N. C., Papaloizou, J., Aug. 1986a. On the tidal interaction between protoplanets and the primordial solar nebula. II - Self-consistent nonlinear interaction. ApJ 307, 395–409.

Lin, D. N. C., Papaloizou, J., Oct. 1986b. On the tidal interaction between protoplanets and the protoplanetary disk. III - Orbital migration of protoplanets. ApJ 309, 846–857.

Meglicki, Z., Wickramasinghe, D., Bicknell, G. V., Oct. 1993. Three-Dimensional Structure of Truncated Accretion Discs in Close Binaries. MNRAS 264, 691–+.

Molteni, D., Belvedere, G., Lanzafame, G., Apr. 1991. Three-dimensional simulation of polytropic accretion discs. MNRAS 249, 748–754.

Molteni, D., Lanzafame, G., Chakrabarti, S. K., Apr. 1994. Simulation of thick accretion disks with standing shocks by smoothed particle hydrodynamics. ApJ 425, 161–170.

Monaghan, J. J., 1992. Smoothed particle hydrodynamics. ARA&A30, 543–574.

Murray, J. R., Mar. 1996. SPH simulations of tidally unstable accretion discs in cataclysmic variables. MNRAS 279, 402–414.

Nelson, R. P., Papaloizou, J. C. B., Jun. 2002. Possible commensurabilities among pairs of extrasolar planets. MNRAS 333, L26–L30.

Okazaki, A. T., Bate, M. R., Ogilvie, G. I., Pringle, J. E., Dec. 2002. Viscous effects on the interaction between the coplanar decretion disc and the neutron star in Be/X-ray binaries. MNRAS 337, 967–980.

Paardekooper, S., Mellema, G., Oct. 2004. Planets opening dust gaps in gas disks. A&A 425, L9–L12.

Papaloizou, J., Lin, D. N. C., Oct. 1984. On the tidal interaction between protoplanets and the primordial solar nebula. I - Linear calculation of the role of angular momentum exchange. ApJ 285, 818–834.

Papaloizou, J. C. B., Sep. 2003. Disc-Planet Interactions: Migration and Resonances in Extrasolar Planetary Systems. Celestial Mechanics and Dynamical Astronomy 87, 53–83.

Papaloizou, J. C. B., Nelson, R. P., Kley, W., Masset, F. S., Artymowicz, P., 2007. Disk-Planet Interactions During Planet Formation. Protostars and Planets V, 655–668.

Perryman, M. A. C., Aug. 2000. Extra-solar planets. Reports on Progress in Physics 63, 1209–1272.

Pierens, A., Nelson, R. P., May 2008. On the formation and migration of giant planets in circumbinary discs. A&A 483, 633–642.

Pringle, J. E., 1981. Accretion discs in astrophysics. ARA&A19, 137–162.

Schäfer, C., Speith, R., Hipp, M., Kley, W., Apr. 2004. Simulations of planet-disc interactions using Smoothed Particle Hydrodynamics. A&A 418, 325–335.

Shakura, N. I., Sunyaev, R. A., 1973. Black holes in binary systems. Observational appearance. A&A 24, 337–355.

Sollins, P. K., Ho, P. T. P., Sep. 2005. The Molecular Accretion Flow in G10.6-0.4. ApJ 630, 987–995.

Speith, R., Kley, W., Feb. 2003. Stability of the viscously spreading ring. A&A 399, 395–407.

Speith, R., Riffert, H., Sep. 1999. The viscous gas ring as an astrophysical test problem for a viscous SPH-code. Journal of Computational and Applied Mathematics 109, 231–242.

Tanaka, H., Takeuchi, T., Ward, W. R., Feb. 2002. Three-Dimensional Interaction between a Planet and an Isothermal Gaseous Disk. I. Corotation and Lindblad Torques and Planet Migration. ApJ 565, 1257–1274.

Terquem, C., Papaloizou, J. C. B., Nelson, R. P., 2000. Disk Evolution towards Planet Formation (Invited Review). In: G. Garzón, C. Eiroa, D. de Winter, & T. J. Mahoney (Ed.), Disks, Planetesimals, and Planets. Vol. 219 of Astronomical Society of the Pacific Conference Series. pp. 19–+.

Udry, S., Santos, N. C., Sep. 2007. Statistical Properties of Exoplanets. ARA&A45, 397–439.

Ulrich, R. K., Dec. 1976. An infall model for the T Tauri phenomenon. ApJ 210, 377–391.

Ward, W. R., Jun. 1997. Survival of Planetary Systems. ApJ 482, L211+.